Journal of Advanced Ceramics
2024, **13**(12): 2068–2086
https://doi.org/10.26599/JAC.2024.9221002

Research Article

Achieving durable double-layered thermal barrier coatings by tailoring multi-scale structures

Guang-Lei Liu†, Lin Zhu†, Xin-Yu Li†, Hussain Sajjad, Xiang-Yu Song, Guang-Rong Li✉, Guan-Jun Yang✉

State Key Laboratory for Mechanical Behavior of Materials, School of Materials Science and Engineering, Xi'an Jiaotong University, Xi'an 710049, China

Received: August 21, 2024; Revised: October 28, 2024; Accepted: November 17, 2024

Abstract: Double-layered thermal barrier coatings (DL-TBCs) have been developed to meet multiple service requirements, such as low thermal conductivity, high thermal stability, and high fracture toughness. Conventional DL-TBCs are often designed on the basis of equal total thickness to have long lifespans, which may weaken the thermal insulation. The reason is that the single-scale designed structure often has opposite effects on the thermal and mechanical properties. To enhance both the thermal insulation and lifespan, this work designed durable DL-TBCs at multiple scales under equivalent thermal insulation. The macroscopic thickness ratio of the top layer to the bottom layer was tailored to optimize the total and single thicknesses, and the microscopic pore size in the top layer was tailored to resist sintering. Six groups of samples with different thickness ratios were prepared. The thermal cycling test revealed that the lifespan of DL-TBCs first increases but then decreases with increasing thickness ratio. The optimized thickness ratio is 2:3 for DL-TBCs, which have the largest lifespan among the six groups. The cross-sectional morphologies revealed that the failure mode changed from the spallation of the top layer to the delamination of the total double layers. The long lifespan of the optimized DL-TBCs stems from the cotailored thickness ratio and porous structure in the top layer to lower the total cracking driving force.

Keywords: thermal barrier coatings (TBCs); double-layered structure; dominant factors; multiscale design; long lifespan

1 Introduction

Thermal barrier coatings (TBCs) have been widely applied in the high-temperature parts of heavy-duty gas turbines to obtain elevated working temperatures and to improve thermal efficiency [1–9]. TBCs usually consist of a top ceramic (TC) layer, a middle bond (BC) layer (including a thermally grown oxide (TGO) layer), and a bottom superalloy substrate (SUB) [10–14]. The ceramic top layer is typically made of 6–8 wt% yttria-stabilized zirconia (YSZ) [3,4,15–18]. However, as the turbine inlet temperature increases (> 1200 °C), the current YSZ TBCs are prone to volume changes [19–21] resulting from phase changes [22,23] and sintering [24–26]. Volume changes in excess often lead to early delamination [27–30], dramatically reducing the lifespan of TBCs. Therefore, advanced TBC materials with better phase stability, higher sintering resistance, lower thermal conductivity, and greater fracture toughness are urgently needed.

To meet the service requirements of TBCs, a variety of new ceramic coating materials have been developed [3,15,31–39]. In terms of these TBC materials, RE-stabilized cubic zirconia (where RE indicates one or more rare-earth elements) is regarded as an alternative ceramic material to YSZ, which has better phase stability and lower thermal conductivity [31–33,40,41]. However, it remains a challenge for new ceramic materials to satisfy all the requirements for TBCs. The advantages of conventional YSZ materials lie in their superior fracture toughness [42–44] and similar coefficient of thermal expansion (CTE) to those of metallic substrates [45]. However, the thermal stability of YSZ is poor [46,47], and its thermal conductivity is relatively high [43,48]. In contrast, new ceramic coating materials have excellent high-temperature phase stability [47,49–52], lower thermal conductivity [31,53–56], better sintering resistance [40], and higher resistance to calcium–magnesium–alumino–silicate (CMAS) corrosion [18,57–68]. Nevertheless, the principle drawback of new ceramic coating materials is their lower fracture toughness (K_{IC}) [40,69,70]. For example, the K_{IC} of rare-earth-stabilized zirconia (RSZ) (RE = Gd, Yb) coating is approximately 1.5 MPa·m$^{1/2}$, which is lower than that of YSZ coatings, with a K_{IC} of ~2.5 MPa·m$^{1/2}$. A lower K_{IC} indicates worse cracking resistance [41]. In addition, CTEs [71,72] for new ceramic materials are often lower than YSZ. The thermal mismatch stress, an important component of the cracking driving force, significantly increases the stress concentration at the interface between the top coat and the bond coat, which promotes cracking and leads to delamination of the coating [73–76]. In addition, compared with YSZ coating, the new ceramic coating is less compatible with TGO, resulting in premature failure in service environments [77–81]. One effective solution to combine the advantages of YSZ and new ceramic coating materials is to use double-layered TBCs (DL-TBCs) [82–89]. The top layer works to prevent heat flux with low thermal conductivity and excellent thermal stability, whereas the bottom layer serves as a stress buffer layer to effectively increase the fracture toughness of the bottom ceramic layer. Therefore, the double-layered structure makes the cracking

† Guang-Lei Liu, Lin Zhu, and Xin-Yu Li contributed equally to this work.

✉ Corresponding authors.
E-mail: G.-R. Li, ligrong@xjtu.edu.cn;
G.-J. Yang, ygj@xjtu.edu.cn

resistance of TBCs competitive with the cracking driving force, mitigating the premature failure of the coating.

To simultaneously meet the service requirements of high-temperature stability, superior thermal insulation, and long lifespan, further design is needed for DL-TBCs [90–92]. Conventional investigations have optimized the macroscopic thickness ratios on the basis of equal total thickness. Dai *et al.* [93] fabricated six groups of DL-TBCs with different thickness ratios based on the same total thickness of 300 μm. The thermal cycling tests revealed that the optimized thickness ratio was 1:1, and their thermal cycling lifespans were ~138.2 and ~1.1 times greater than those of the single-layer top and bottom coatings, respectively. A similar optimized thickness ratio can also be obtained from Liu *et al.* [94]. Mahade *et al.* [95] prepared three groups of DL-TBCs with different thickness ratios on the basis of a total thickness of 500 μm. The thermal shock test results revealed that the samples with a thickness ratio of 1:1 presented the highest lifespan, which was approximately 1.2 times greater than that of the samples with a thickness ratio of 1:4. Zhu *et al.* [96] employed fracture mechanics to analyze the extension of cracks at the interface of DL-TBCs under different geometrical parameters and porosity conditions. The results of this analysis indicated that the sample with a thickness ratio of approximately 1:1 exhibited the lowest strain energy release rate (SERR). In particular, DL-TBCs are prone to failure at weak interfaces [97–100], which are usually located at the interface of two adjacent ceramic layers. Therefore, improving the thermophysical properties of the interlayer interface, for example, by incorporating a transition layer (TL) [101,102], can significantly improve the performance of the coating. Liu *et al.* [101] prepared TLs in DL-TBCs, which effectively reduced the stress concentration between the ceramic layers. This resulted in an extended thermal cycling lifespan of DL-TBCs with TLs of ~9.2% compared with that of DL-TBCs without TLs. Shen *et al.* [102] fabricated a gradient transition layer (GTL) with elemental gradient variations at the interface of two adjacent ceramic layers. The introduction of GTL in the double-layered structure can avoid the drawbacks associated with the instability of the interface between ceramic layers [97]. The thermal cycling lifespan of DL-TBCs with GTL was found to be 35.6% longer than that of DL-TBCs without GTL.

A question for the aforementioned DL-TBCs [93–96] is that they were mostly designed and prepared on the basis of a single scale and equal total thickness, which leads to difficulties in ensuring high thermal insulation for the optimized DL-TBCs throughout their lifespans at the same time. The causes are at least twofold. On the one hand, the two layers have different thermal and mechanical properties [103–105], suggesting that a change in thickness may have opposite effects on thermal insulation and lifespan. For example, a decrease in the thickness of the top layer may enhance the fracture resistance of the total DL-TBC, but weaken the thermal insulation [106,107]. As a result, the optimized lifespan of DL-TBCs may involve different types of thermal insulation. On the other hand, microstructural changes during thermal exposure have a substantial impact on the thermal and mechanical properties of a material [108–111]. The primary microstructural change is the sintering of the ceramic layer [24,25]. The ceramic coatings prepared by plasma spraying (PS) contain substantial interlamellar two-dimensional (2D) pores with opening widths usually smaller than 100 nm [112]. This typical lamellar structure significantly affects the thermal and mechanical properties of such coatings. For example, the thermal conductivity and elastic modulus of a PS-YSZ coating are usually 1/3 less than those of the corresponding bulk materials [112–115]. After thermal exposure, this lamellar structure gradually heals and disappears, resulting in a dramatic increase in its thermal conductivity and elastic modulus [116–119]. The former decreases the thermal insulation, whereas the latter increases the thermal mismatch stress [98–100]. Consequently, the coating sintering behavior may cause degradation in both thermal insulation and strain tolerance [24,120]. Therefore, further optimization of DL-TBCs is required to balance and enhance the thermal and mechanical properties.

In this study, unlike conventional single-scale and total-thickness bases, we designed DL-TBCs with multiscale structures based on equivalent thermal insulation to enhance both the thermal insulation and lifespan. The macroscopic thickness ratio and microscopic porous structure in the top layer were tailored and optimized via an isothermal thermal cycling test. The microstructures and mechanical properties were characterized to comprehensively investigate the thermal cycling behavior of DL-TBCs. Finally, the performance enhancement mechanism of the optimized DL-TBCs was elucidated on the basis of the theoretical and experimental results. This work is expected to provide a better understanding of achieving durable DL-TBCs by tailoring multiscale structures to accelerate the engineering application of thermal protection coatings used in heavy-duty gas turbines.

2 Experimental

2.1 Design of a coating architecture with a multiscale strategy

To further explore the performance potential of the coating, a multiscale structural design was proposed for DL-TBCs. The thickness ratio between the two layers varied at the macroscopic scale, whereas the pore structure in the top layer was tailored at the microscopic scale.

In our previous study, unit thermal resistance (UTR) was used to evaluate the thermal insulation performance of TBCs, as shown in Eq. (1) [98]:

$$\mathrm{UTR} = \frac{\delta}{\lambda} \tag{1}$$

where δ is the thickness of the ceramic coating and λ is the thermal conductivity.

In this work, RSZ ($5Gd_2O_3$–$5Yb_2O_3$–$10Y_2O_3$–$80ZrO_2$, wt%) was used to prepare the top layer, and YSZ was used to prepare the bottom layer. Codoping with the rare earth element Gd–Yb–Y significantly reduces the thermal conductivity and improves the thermal phase stability of ZrO_2 [121–124]. For DL-TBCs, UTR of the double layers is the sum of each layer. Hence, UTR of YSZ/RSZ DL-TBCs can be expressed as Eq. (2):

$$\mathrm{UTR} = \frac{\delta_{\mathrm{YSZ}}}{\lambda_{\mathrm{YSZ}}} + \frac{\delta_{\mathrm{RSZ}}}{\lambda_{\mathrm{RSZ}}} \tag{2}$$

where δ_{YSZ} and δ_{RSZ} are the thicknesses of YSZ and RSZ coatings, respectively. λ_{YSZ} and λ_{RSZ} are the thermal conductivities of YSZ and RSZ coatings, respectively.

The thermal conductivity of atmospheric plasma spraying (APS)-YSZ coating at 1000 °C is 1.21–1.35 $W{\cdot}m^{-1}{\cdot}K^{-1}$ [15,125], whereas the thermal conductivity of the RSZ coating is only 0.85 $W{\cdot}m^{-1}{\cdot}K^{-1}$ [15]. The thermal conductivities of APS-RSZ and YSZ coatings are 1.0 and 1.2 $W{\cdot}m^{-1}{\cdot}K^{-1}$, respectively, which were measured in this work at 1000 °C. Therefore, if the thermal insulation effect of the 100 μm thick YSZ coating is defined as 1 unit, the 83 μm thick RSZ coating has exactly the same thermal

insulation effect as the 1 unit. According to the analysis above, six groups of TBCs with similar thermal insulation performances from both macroscopic thickness and microstructural perspectives were designed in this study. Figure 1 shows a schematic diagram of the top coating architecture, namely, 250 μm YSZ (5Y), 200 μm YSZ+42 μm RSZ (4Y/1R), 150 μm YSZ+83 μm RSZ (3Y/2R), 100 μm YSZ+125 μm RSZ (2Y/3R), 50 μm YSZ+167 μm RSZ (1Y/4R), and 208 μm RSZ (5R). DL-TBCs design is beneficial for reducing the top ceramic coating thickness. Moreover, to tailor the microscopic pore structure in RSZ coating, massive incompletely melted agglomerated nanoparticle stacks were introduced into RSZ coating by modulating the spraying process parameters, as shown in Fig. 1.

2.2 Preparation of DL-TBCs and RSZ splats

To fabricate TBCs with different porous structures, hollow spherical 8YSZ (Metco 204B-NS, 45–75 μm) and solid subspherical RSZ (45–75 μm) are used to deposit the ceramic top coat via an APS system, as shown in Fig. 2. The structure deposited from RSZ often has a higher porosity and is more resistant to sintering than that deposited from YSZ. A laser diffraction particle size analyzer (Mastersizer 2000, Malvern Instruments Ltd., UK) was used to evaluate the size distribution of the powders. The morphology and particle size distribution of YSZ powder and RSZ powder are shown in Fig. 2. APS parameters for the top coat are shown in Table 1. Prior to the deposition of the top coat, a commercially available NiCoCrAlTaY powder (Amdry 997, Oerlikon Metco, Switzerland) was used as the bond coat and deposited on a nickel-based superalloy (Inconel 718, ϕ25.4 mm × 3 mm) substrate. The bond coat was deposited to approximately 150 μm by a high-velocity oxygen fuel (HVOF) system. Before the deposition of the top coat, the as-prepared samples with the bond coat were subjected to a preheating treatment to form a dense and connected Al_2O_3 TGO, which could lower the thickening rate of TGO and reduce the stress from TGO growth to increase the high-temperature oxidation resistance and extend their service lifespans [126–128]. The preheating-treatment process consists of two steps, conducted in a furnace (PCO-1200A, Xi'an Jiaotong University, China) with finely controlled oxygen partial pressure. In the first step, the samples were pre-diffused at 1000 °C for 4 h with a controlled oxygen partial pressure below 0.01 ppm, and in the second step, the pre-diffused samples were pre-oxidation at 1080 °C for 4 h with a controlled oxygen partial pressure below 10 ppm. Additionally, on the basis of our previous research on the mechanism of process factors on the thermophysical and mechanical properties of RSZ coatings, a mapping law between the preparation process and the microstructure (e.g., unmelted region/unmelted or partly melted agglomerated nanoparticle stacks) was obtained.

To observe and characterize the structure and sintering behavior of the samples, the same parameters were used to deposit the double-layered ceramic coatings on the stainless steel substrates without a bond coat. Free-standing samples were obtained by dissolving the substrate in a hydrochloric acid solution followed by further immersion in deionized water for 24 h, with the aim of removing residual acid from the coating.

A plasma-sprayed coating was formed by stacking individual splats. Therefore, the interlamellar pore surface refers to the splat surface. To investigate the roughening behavior of the pore surface, RSZ powder was used to deposit individual splats [129]. The individual RSZ splats were deposited on polished ceramic pellets made up of ZrO_2 (Bai-Le Inc., China) to avoid the oxidation effect of the metal substrate during thermal exposure. Before the splats were deposited, the surface of the substrate was preheated to approximately 300 °C to obtain a disk-shaped RSZ splat [130].

2.3 Characterization of microstructure and properties

The service temperature of TBCs for gas turbines (e.g., F-class land-based gas turbines) is ~1000 °C, with a lifetime of approximately 8000–24,000 h [131]. To speed up the testing, the samples and the as-deposited ceramic splats were heated in a furnace (SX-Q08163, Tianjin Zhonghuan Electric Furnace Co. Ltd., China) to temperatures ranging from 1300 to 1500 °C. The samples were held at the heating temperature for progressively increasing durations, after which they were cooled to room temperature (RT). The heating and cooling rates were fixed at a relatively low rate of 10 °C·min^{-1}.

A scanning electron microscope (SEM; MIRA 3, TESCAN, Czech Republic) was used to characterize the surface and cross-sectional morphology of the samples. The phase compositions of RSZ coatings and YSZ coatings before and after the thermal cycling test were characterized via an X-ray diffractometer (XRD;

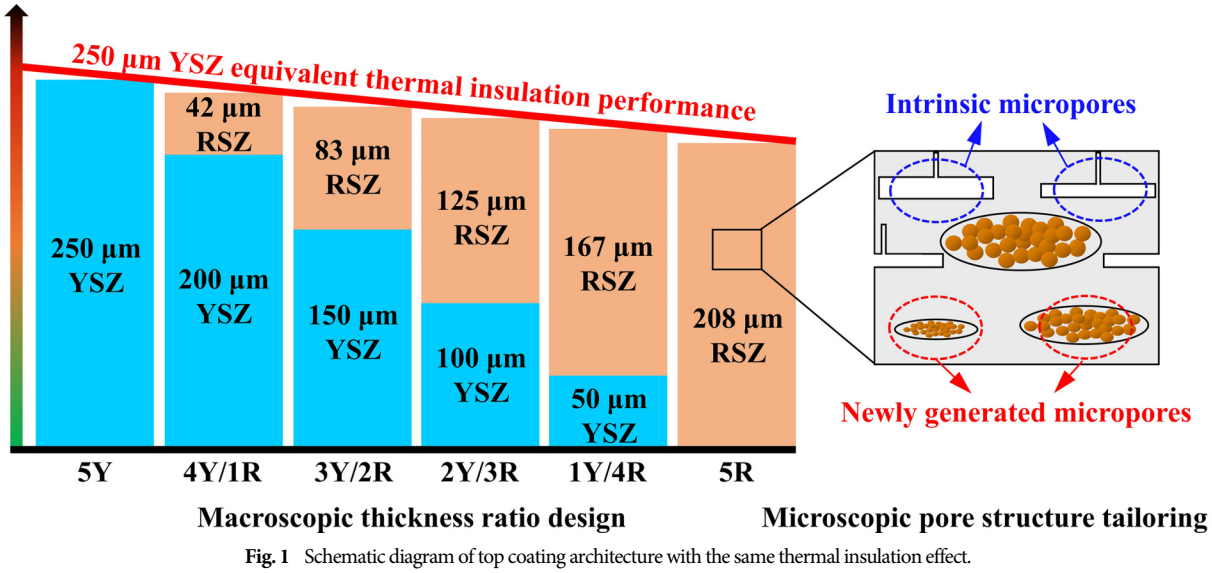

Fig. 1 Schematic diagram of top coating architecture with the same thermal insulation effect.

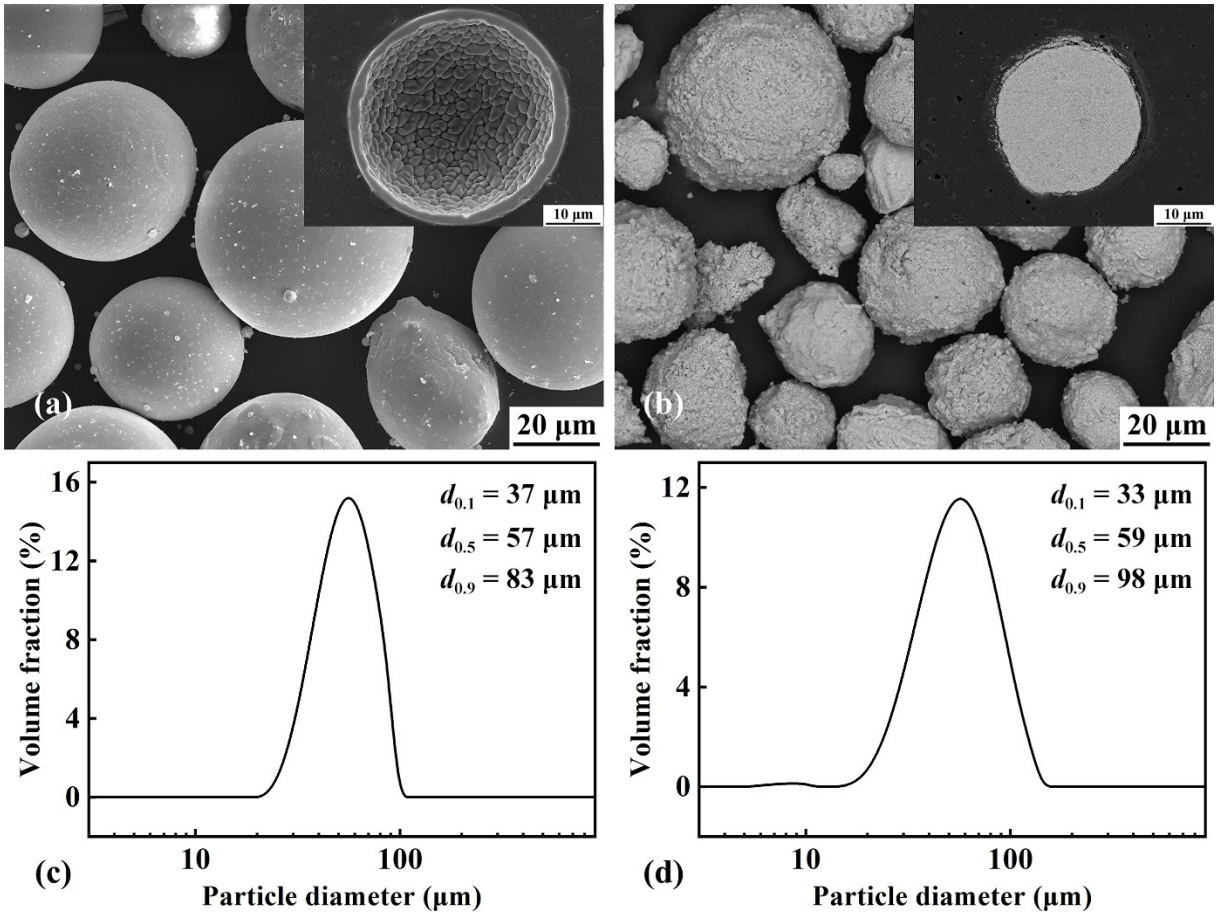

Fig. 2 Morphology and particle size distribution of (a, c) spherical 8YSZ and (b, d) RSZ powder used for top coating.

Table 1 APS parameters

Parameter	YSZ	RSZ
Arc current (A)	650	640
Arc voltage (V)	65	63
Plasma gas (Ar) flow (L·min^{-1})	50	45
Plasma gas (H_2) flow (L·min^{-1})	7	7
Spray distance (mm)	100	100

D8 Advance, Bruker, Germany). The porosity and unmelted region proportion of the coatings were estimated via SEM backscattered electron (BSE) images. For each state during thermal exposure, 10 images were used. Porosity was obtained by binarizing BSE images with ImageJ 1.45 software [24]. The key to obtaining the unmelted region proportion is to specify its outer contour boundary with the software. 2D pores were examined via two methods. One is quasi-*in situ* observation via SEM, and the other is quantitative characterization via statistical 2D pore density. The details of these two methods can be found elsewhere [120,132]. According to a previous study on the coating bonding ratio [112], the unbonded ratio of the coating contributed by 2D pores can be calculated according to Eqs. (3) and (4):

$$L_2 = \frac{H \cdot L_2}{\delta} \tag{3}$$

$$\varepsilon = \frac{\xi \cdot H \cdot L_1}{L_2} = \xi \cdot \delta \tag{4}$$

where ξ is the 2D pore density, H is the coating thickness, L_1 is the coating length, L_2 is the total length of the interface between splats in the coating, δ is the splat thickness, and ε is the unbonded ratio contributed by 2D pores.

The morphology of the splat surface during thermal exposure was characterized via an atomic force microscope (AFM; SPM-9700HT, Shimadzu, Japan). The topography and cross-sectional profile of the splat surfaces were analyzed via NanoScope Analysis software (SPM-9700HT, Shimadzu, Japan).

The cross-sectional Vickers hardness was determined with a micro-Vickers indenter (Buehler Micromet 5104, Akashi Co., Japan). The hardness test was performed at a test load of 300 gf and a holding time of 30 s. The in-plane Young's modulus of the top coating was measured via the Knoop indentation method. The parameters and test system used were the same as those used for the measurement of microhardness. The formula for determining the elastic modulus is shown in Eq. (5):

$$E = \frac{\alpha H_V}{\frac{b}{a} - \frac{b'}{a'}} \tag{5}$$

where α is a constant (0.45), H_V is the micro-Vickers hardness, a' and b' are the lengths of the major and minor diagonals of the indentation impression, respectively, and a and b are the lengths of the major and minor diagonals of the indenter, respectively.

The thermal conductivity was determined via a laser flash method. The sample size was ϕ12.7 mm × 1.2 mm, which was measured via a micrometer (DL9325, Deli, China). A laser flash analysis equipment (FL 5000, Amtek, USA) was used to determine the thermal diffusivity of the coating in the temperature range from 200 to 1500 °C in an air atmosphere. A differential scanning calorimeter (DSC 404, Netzsch, Germany) was used to

determine the heat capacity of the coating. The density was calculated by dividing the mass of the samples by their volume. The sample volume was determined through the Archimedes drainage method with a densitometer (ET-320-2291, Etnaln, China). The tests were performed 3 times on each sample at different positions to reduce errors. The thermal conductivity can subsequently be calculated via Eq. (6) [133]:

$$\lambda = \alpha \cdot c_p \cdot \rho \tag{6}$$

where λ is the thermal conductivity of the material, α is the thermal diffusivity, c_p is the specific heat capacity, and ρ is the density.

2.4 Thermal cycling test for DL-TBCs

The turbine blade in service can be equated to a thermal shock test. TBCs surface is subjected to flame thermal shock, and the backside substrate is cooled by cooling airflow. As a result, the blade surface temperature can reach or even exceed 1300 °C, but the temperature of the substrate side is ~1000 °C [98,99]. An isothermal thermal cycling test (SGM9813DE, Luoyang Sigma High-Temperature Electric Furnace Co., Ltd., China) was used to evaluate the lifespan of TBCs. In this test, both the coating and the substrate were heated to the same temperature. A temperature of 1050 °C was chosen as the test temperature because the substrate cannot withstand temperatures that are too high [134–136].

For each cycle, TBCs samples were heated to 1050 °C in 5 min, held for 50 min, and then cooled to 80 °C or lower in 5 min by forced cooling. The lifespan of TBCs was defined as the thermal cycling lifecycles when 20% area delamination or spallation of the top coating was observed.

3 Finite element simulation

3.1 Model geometry

Finite element method (FEM) is a very effective method for exploring the stress distribution and crack propagation behavior in coatings and has been implemented by many researchers [30,137,138]. In this study, a thermal cycling model is developed to assess the effects of continuous stiffening on the stress distribution and crack driving force, as shown in Fig. 3. TBCs models consist of a ceramic top coating with two layers, a TGO layer, a BC, and a SUB. The crack length is finally chosen as 5 μm through evaluation of the cracking driving force under different interfacial delamination lengths. The crack distance from the top coating surface is h. Since different groups of TBCs possess different thicknesses of RSZ and YSZ layers, the thickness of the top coating is not constant for all groups of TBCs. The thicknesses of SUB (h_{SUB}), BC (h_{BC}), and TGO (h_{TGO}) layers are 3, 0.15, and 0.001 mm, respectively. TGO interface roughness is simplified by an ideal cosine interface model, and its vertical position y can be expressed as $y(x) = A \cdot \cos(2\pi x/L)$, where x is defined as the coating's longitudinal direction, the amplitude A is 25 μm and the wavelength L is 100 μm. Importantly, some cases were simplified in these models to focus on the effects of the macroscopic thickness ratio and stiffening. The primary simplification is that the TGO layer thickens throughout the dwelling [30,139,140].

3.2 Boundary conditions

On the basis of the above description, the model has a feature of periodic symmetry. Therefore, any periodic part can be used to describe the whole structure with proper periodic boundary

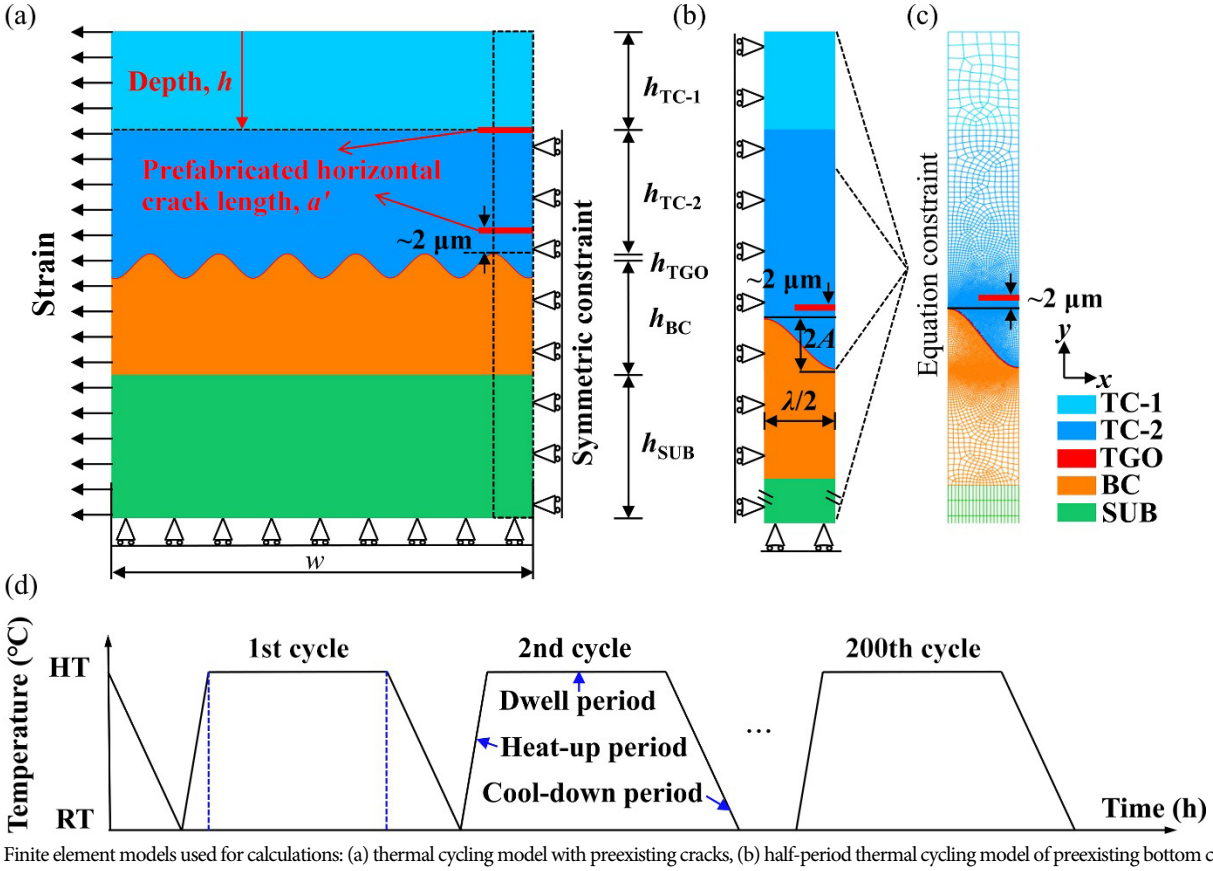

Fig. 3 Finite element models used for calculations: (a) thermal cycling model with preexisting cracks, (b) half-period thermal cycling model of preexisting bottom cracks, (c) half-period thermal cycling model meshing of preexisting bottom cracks, and (d) thermal cycling history for TBCs model.

conditions. In this work, a periodic pattern was cut from the whole structure, as shown in Fig. 3(b). One half-crack was inserted at the right boundaries of the half-period pattern.

Finite element simulations were performed via the commercial software ABAQUS 6.14. For the thermal cycling model with periodic properties, only half of its periodic model needs to be calculated in ABAQUS. The regions near the TGO layer and the crack interface were refined to ensure that the crack extension was not influenced by the mesh size. The left side of the thermal cycling model uses a symmetric boundary condition that restricts its movement along the *x*-axis. This symmetric boundary condition simulates the behavior of the real structure under symmetric loading by restricting the degrees of freedom of the model translation along the *x*-axis, thus reducing the amount of computation and improving the efficiency of the analysis. The right side uses a periodic boundary condition (equation constraints) [30,141], whereas previous studies have mostly used multipoint constraint (MPC) constraints [142,143]. MPC allows the imposition of constraints among different degrees of computational model freedom, while the equation constraints define the relationships among nodes by means of mathematical equations, which is a more flexible way to express more complex constraint relationships. To avoid rigid body displacement, the bottom side is restricted to move along the *y*-axis. Figure 3(c) shows the full model mesh divided by a four-node plane strain cell.

3.3 Material parameters

All parts of the model are set to be isotropic and homogeneous. Upon loading, SUB and TC layers exhibit elastic behavior, whereas BC layer behaves as an elastic–plastic material. At room temperature, the yield strength of BC is 868 MPa [141]. The change in yield strength is subsequently nearly linear as a function of temperature. The creep behavior of all the layers is not considered in this study. The reason is that it has no obvious effect on the general trends in this study. Moreover, TC creep behavior is not as obvious for thermal cycling with a short dwell time (e.g., 50 min in this study) at high temperature (HT). The temperature-dependent parameters of TC, BC, and SUB can be found in previous studies [80,144].

3.4 Dynamic stiffening control in thermal cycling loading

TBCs were subjected to thermal cycles, including heating, holding, and cooling stages. As a result, TBCs are repeatedly loaded due to the substrate constraint. Figure 3(d) shows the total thermal cycling process. The initial stress-free state of the system starts at an HT, as reported in previous investigations [30,145]. The reason is that most stresses are relaxed through plastic deformation. When the system is cooled to room temperature, the stress increases to a certain value that is comparable to the residual stress during deposition. Subsequently, thermal cycles were applied to the system [146]. To clarify the effect of continuous stiffening on the stress distribution in the coating, a continuous stiffening subroutine [141] was embedded in the thermal cycling model. To simulate the dynamic stiffening of TBCs during actual thermal cycling more realistically, the experimental thermal cycling data were set as the thermal cycling loading parameters of the model in this study.

3.5 Description of crack propagation

Since SERR is based on the conservation of energy, it is less dependent on the stress singularity at the crack tip. Accordingly, SERR is very suitable for evaluating the cracking driving force in this TBCs system, which was calculated via the virtual crack closure technique (VCCT) [99].

4 Results

4.1 As-sprayed structure of DL-TBCs

Following the equivalent thermal insulation design strategy, we fabricated six groups of YSZ/RSZ DL-TBCs with different thickness ratios. The free-standing TBCs thicknesses met the design criteria, and all the layers contained abundant 2D unbonded interlamellar interfaces, interlamellar microcracks, and three-dimensional spherical pores (Figs. 4(a)–4(f)). The cross-sectional morphology of the RSZ coating shows typical splat stacking and nanoparticle stack features (Fig. 4(g)). RSZ coating results in a greater porosity and unmelted region proportion than does YSZ coating under thermal exposure (Fig. 4(h)), specifically in the initial state, in which the porosity and unmelted region proportions of RSZ coating are 9.5%±0.2% and 25.6%±1.8%, respectively, and those of YSZ coating are 8.0%±0.1% and 8.6%±1.3%, respectively. This difference can be attributed to two factors: the intrinsically high melting point of RSZ coating and the differential sintering effect introduced by the agglomerated nanoparticle stacks, which reduces the degree of pore healing during sintering and enhances the sintering resistance of the coating.

4.2 Failure modes and thermal cycling lifespan of DL-TBCs

We then observed the cross-sectional morphology of the six groups of DL-TBCs after thermal cycling failure to clarify the failure modes on the basis of the spalling behavior of the top ceramic coating. Although the microscopic pore structures in the coatings prepared via the same process are relatively similar, the failure mode changes from spallation of the top layer to delamination of the total double-layered structure with increasing thickness ratio (Figs. 5(a)–5(f)), indicating that the size effect results from the thickness ratio. This leads to an approximately normal distribution feature of TBC thermal cycling lifespan (Fig. 5(g)). YSZ/RSZ DL-TBCs with a thickness ratio of 150/82 (3Y/2R) have the highest thermal cycling lifespan of 690±9 cycles, which is approximately double and nineteen times greater than those of pure YSZ and RSZ coatings, respectively. This can be attributed to the macroscopic thickness ratio design, which delays RSZ coating spalling and maximally reduces the elastic modulus of the entire ceramic coating owing to the microscopic pore design in RSZ layer. Under the prerequisite that RSZ layer does not spall, decreasing the double-layer thickness ratio while minimizing the TBC thickness within a certain range allows maintaining the elastic modulus and the thickness of the total ceramic coating at an extremely low level, which is attributed to reducing the cracking driving force with the same crack resistance, thus greatly improving the thermal cycling lifespans of YSZ/RSZ DL-TBCs.

5 Discussion

5.1 TGO thickening induced by exposure to high temperatures

Since TGO thickening is considered one of the significant causes

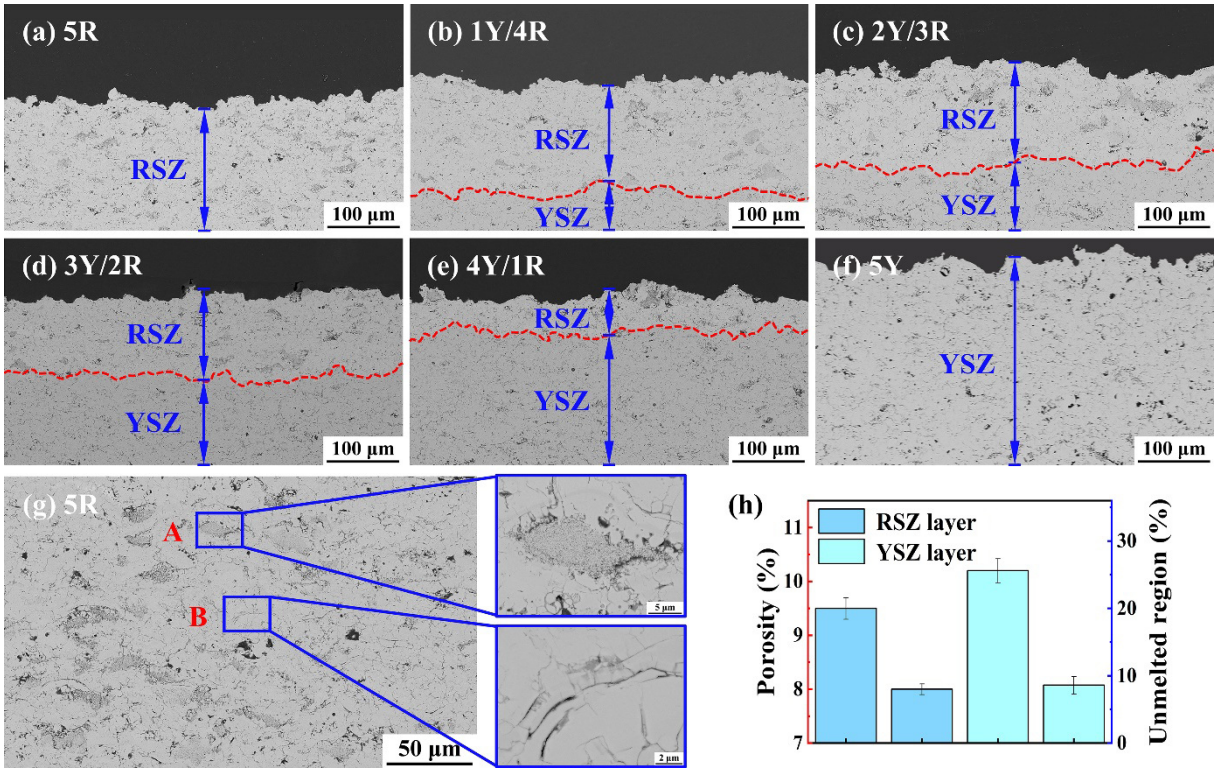

Fig. 4 Cross-sectional morphology of (a–f) six groups of RSZ/YSZ DL-TBCs and (g) pure RSZ coating (5R). (h) Apparent porosity of RSZ and YSZ coating.

leading to the failure of TBCs [79,81], we observed TGO cross-sections of the failure samples.

After failure, TGO layer consisted of an upper gray phase and a lower black phase, as shown in Fig. 6(a). According to EDS results in Table 2, the black oxides were mainly Al_2O_3, whereas the gray oxides were mainly mixed oxides of Ni, Co, Cr, Al, and O. In addition, the formation of mixed oxides is attributed to the fact that the consumption of Al promotes the outward diffusion of other metal elements [147–149]. Liu *et al.* [150] reported that the evolution of TGO layer follows this sequence from the original phase to α-Al_2O_3+Cr_2O_3 and then to mixed oxides of α-Al_2O_3+Cr_2O_3+Ni(Al,Cr)$_2O_4$ and NiO. In this work, the composition of TGO layer developed from the original phase to mixed oxides during oxidation.

Although the mixed oxides appeared at TGO edge due to aluminum depletion (Fig. 6(a)), SEM-BSE images still distinctly revealed TGO morphology. The average thickness of TGO was evaluated in five different regions for each sample after failure (Fig. 6(b)). TGO thicknesses of 3Y/2R, 4Y/1R, and 5Y groups range from 5.03–6.71 μm, which are significantly close to the reported critical thickness of 5–6 μm [79], whereas the remaining three groups exhibit TGO thicknesses less than 5 μm. This result proves that significant thickening of TGO is one of the dominant factors responsible for the failure of TBCs in this study.

5.2 Phase transformation induced by high-temperature thermal exposure

To verify whether the phase transformation also contributes to failure, we performed XRD analysis to characterize the phase composition of the top coating after thermal cycling failure (Fig. 7). In the as-sprayed state, XRD pattern of YSZ coating has a monoclinic phase (M phase) at 27° and 32° according to PDF card (No. 37-1484). Moreover, there was no monoclinic phase but rather a tetragonal phase/metastable tetragonal phase (T/T′ phase, PDF card No. 50-1089) and a cubic phase (C phase, PDF card No. 49-1642) in RSZ coating. The addition of Gd_2O_3 (PDF card No. 24-0430) and Yb_2O_3 (PDF card No. 74-1981) could replace some of Y_2O_3 (PDF card No. 20-1412) and improve the stability of ZrO_2 [41]. No obvious phase transition was observed in RSZ coating after 690 cycles at 1050 °C (Fig. 7(b)), and the main phase was the cubic phase [40,122,124]. The phase compositions of YSZ coating were a monoclinic phase, a cubic phase, and a small metastable tetragonal phase with phase transformation after the thermal cycling test [22] (Fig. 7(a)). In the as-sprayed state, the peaks of the monoclinic and cubic crystal systems were small, and neither of them increased significantly compared with those of the coatings after the thermal cycling test. Therefore, the phase transformation is not responsible for the failure of DL-TBCs.

5.3 Sintering-induced stiffening during thermal exposure

On the basis of the findings of Lima and Marple [151], Zhang *et al.* [111], and Li *et al.* [24,29,152], the RSZ coating prepared in this study has a nanobimodal structure consisting of alternately distributed dense splats and porous agglomerated nanoparticle stacks, with the former formed by the deposition of completely melted splats and the latter stemming from the formation of unmelted or partly melted agglomerated nanoparticles, which have different sintering behaviors. Compared with splats, stacks have a greater sintering driving force and a higher sintering contraction rate, accounting for the smaller grain size and larger specific surface area of the agglomerated nanoparticles. The sintering contraction rate of the stacks is greater than that of the splats after thermal exposure. This leads to a differential sintering phenomenon, which creates new large-scale pores at the interface between the two, increasing the porosity and exerting a substantial effect on the cracking driving force of the double-layered structure.

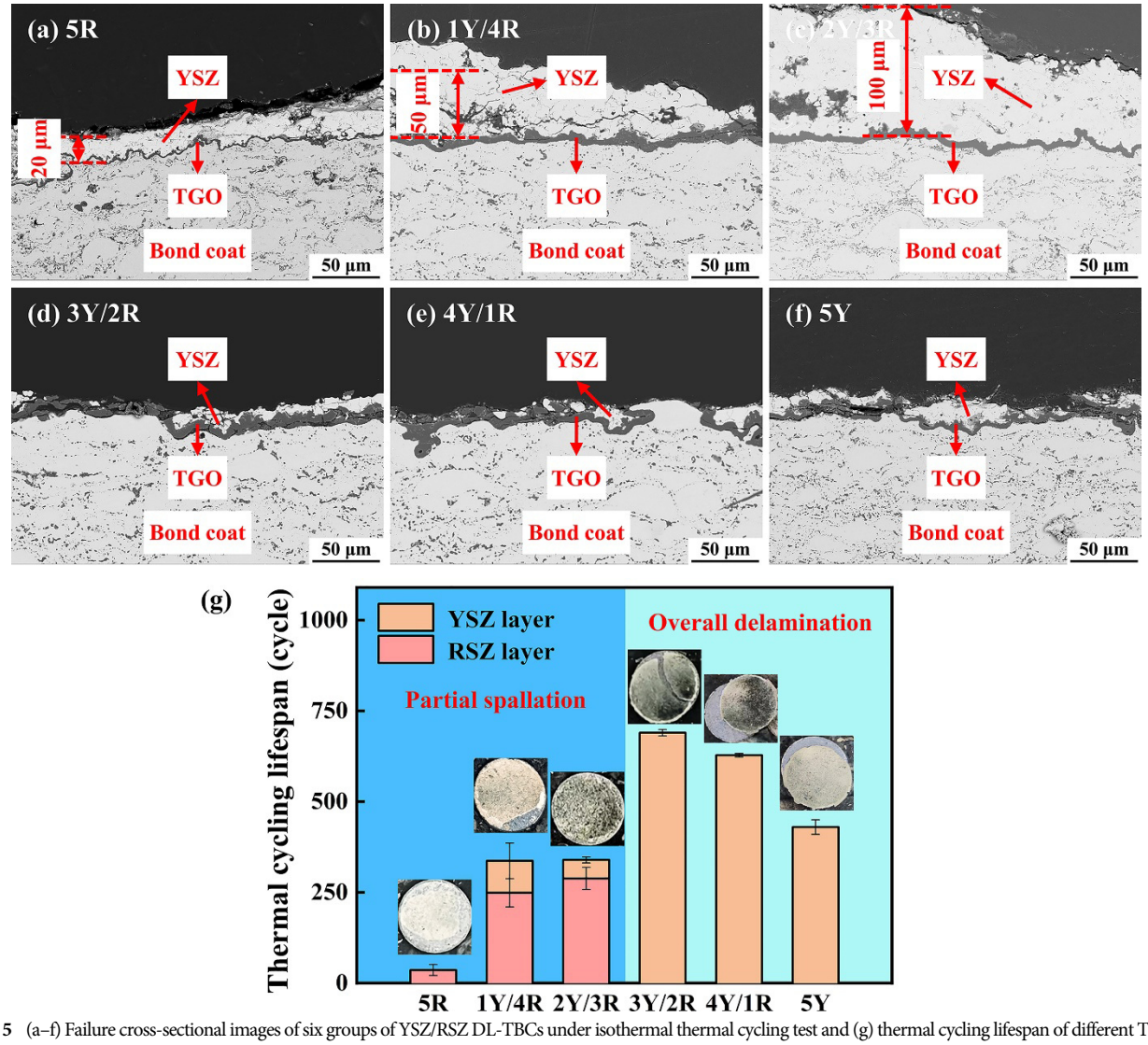

Fig. 5 (a–f) Failure cross-sectional images of six groups of YSZ/RSZ DL-TBCs under isothermal thermal cycling test and (g) thermal cycling lifespan of different TBCs.

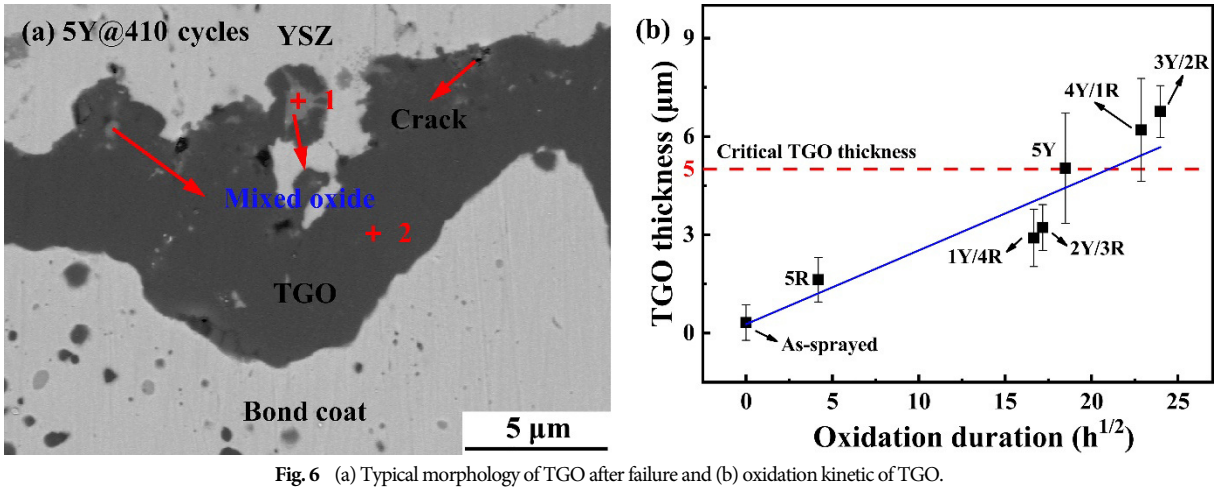

Fig. 6 (a) Typical morphology of TGO after failure and (b) oxidation kinetic of TGO.

Table 2 EDS results for different regions in Fig. 6(a) (Unit: wt%)

Region	Ni	Co	Cr	Al	O	Y
1	15.92	13.62	17.06	18.49	24.77	0.00
2	8.16	4.65	0.00	49.09	36.55	0.00

5.3.1 *Pore morphology evolution during thermal exposure*

The differential sintering behavior after thermal exposure of RSZ coating with a nanobimodal structure requires careful examination of the microscopic pore morphology and the associated underlying mechanisms. We first performed SEM-BSE

on the polished cross-section of the as-sprayed coating to evaluate the structural characteristics. Overall, the as-sprayed coating has a bimodal structure consisting of a dense matrix and massive incompletely melted agglomerated nanoparticle stacks (Figs. 8(a) and 8(d)). Moreover, the apparent porosity, interlamellar 2D pore density, and unbonded ratio contributed by the 2D pores (δ = 1.5 μm) of the as-sprayed coating are 9.5%±0.2%, 0.25±0.03 μm·μm^{-2}, and 0.37, respectively (Figs. 8(g)–8(l)). In particular, Fig. 8(g) shows the change in apparent porosity. After the first 5 h of exposure, the apparent porosity decreases from approximately 12.2%±0.5% for the as-sprayed coating to nearly 8.8%±0.2%. During further exposure, the rate of decrease slows, and when the exposure duration reaches 200 h, the apparent porosity decreases to 6.6%±0.3%. These results indicate that sintering of RSZ coating occurred during exposure, leading to densification of the RSZ coating.

To reveal the effect of thermal exposure on the pore morphology, we characterized the cross-sections of the RSZ

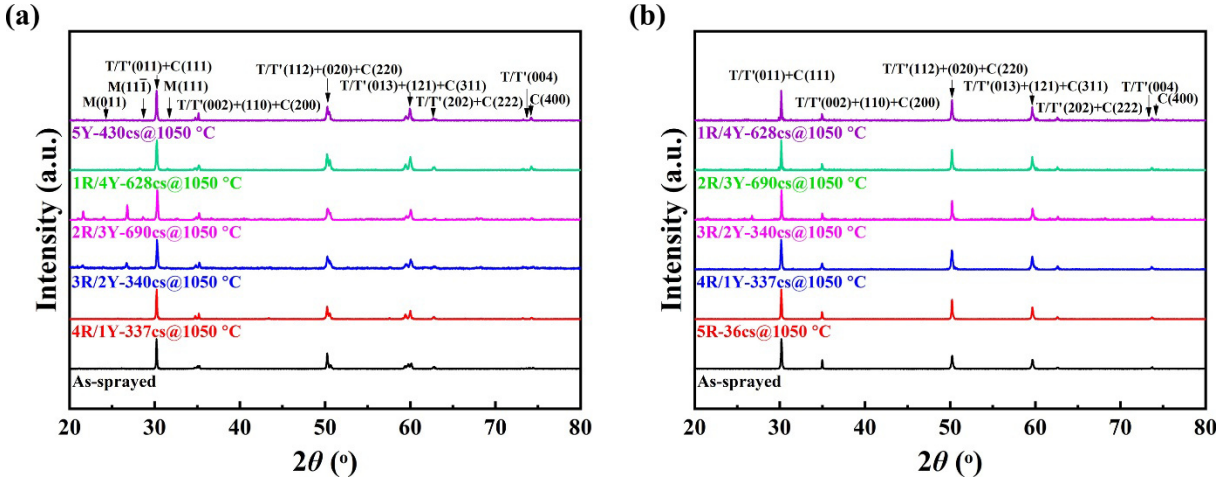

Fig. 7 XRD patterns of top coating before and after thermal cycling test: (a) YSZ and (b) RSZ.

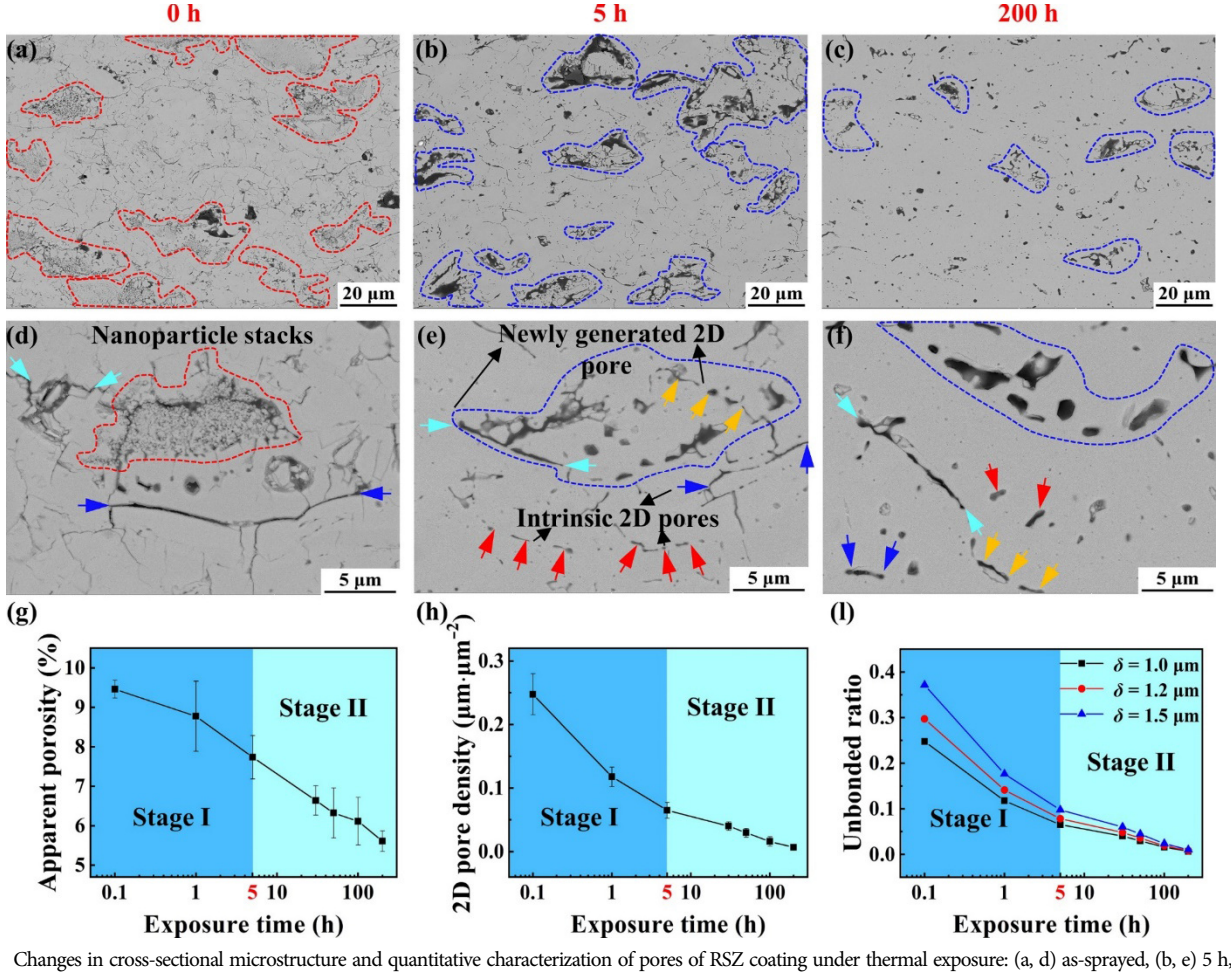

Fig. 8 Changes in cross-sectional microstructure and quantitative characterization of pores of RSZ coating under thermal exposure: (a, d) as-sprayed, (b, e) 5 h, and (c, f) 200 h. Effect of thermal duration on (g) apparent porosity, (h) residual 2D pore density, and (l) unbonded interface ratio contributed by 2D pores.

coating after different durations (Figs. 8(b), 8(c), 8(e), and 8(f)). The logarithmic plots reveal that the changes in the apparent porosity and the residual 2D pore density are stage sensitive (Figs. 8(g) and 8(h)). At stage I (< 5 h), the healing kinetics of the intrinsic pores in the matrix and the new pores introduced by the particle stacks (Figs. 8(b) and 8(e)) are considerably faster. The intrinsic interlamellar 2D pores in the matrix with narrow gap widths were segmented into several smaller regions, accounting for the grain bridging, and a few pores with large opening widths remained (Fig. 8(e)). Numerous newly generated lamellar pores formed along the particle-stack/matrix interface (Fig. 8(b)), whereas the number of spherical pores in the stacks rapidly decreased (Fig. 8(e)). In contrast, at Stage II, most pore structure changes tended to stabilize, and only the pore morphology evolved since the unhealed parts were relatively wider (Figs. 8(c) and 8(f)).

During sintering, the surface energy can restrict the growth of the grains in a coating by altering the activation energy of the grain growth (Q), which plays a key role in increasing the grain size [153]. The grain growth kinetics were calculated via Eq. (7):

$$D_t = D_0 \cdot \exp\left(\frac{-Q}{R \cdot T}\right) \tag{7}$$

where D_0 and D_t are the initial and final crystallite sizes, R is the molar gas constant, and T is the thermal exposure temperature.

The obtained activation energy of the grain growth was approximately 10 kJ·mol^{-1} [29]; the corresponding energy for the bulk material was approximately 580 kJ·mol^{-1} [153]. Therefore, the considerably low grain growth activation energy is most likely responsible for the differential sintering between the matrix and the nanoparticle stacks. These coarse voids can counteract the negative effect of the healing of microscopic pores.

5.3.2 *Evolution of interlamellar pores on fracture cross-section during thermal treatment*

To gain deeper insight into the role of gap width in pore healing, we focused on the healing behavior of the intrinsic and newly generated interlamellar 2D pores. Unlike stage I pores, most interlamellar 2D pores only underwent morphological changes in stage II owing to the reduction in multipoint contact healing, whereas the residual 2D pores exhibited larger opening widths [130]. In principle, the interlamellar pores in conventional coatings continue to heal with decreasing gap width during sintering [130]. However, the nanobimodal-structured coating has a different interlamellar pore evolution due to the introduction of new 2D pores by the stacks [111]. Thus, the critical pore healing width can provide a window for understanding the role of gap width in the sintering of nanobimodal structure coatings. Figure 9 shows the quasi-in situ interlamellar pore morphology after different durations (Figs. 9(a)–9(c)), a schematic of the evolution of the intrinsic interlamellar 2D pores (Fig. 9(d)), and the evolution of the newly generated interlamellar 2D pores (Fig. 9(e)). Further characterization of the coating cross-sections after different durations by SEM-SE reveals that the flat splat surface gradually becomes rough after thermal exposure, leading to multipoint contacts at the narrow pore edges, which provides multiway diffusion for matter transfer (Fig. 9(b)). The nanoparticle stacks experience differential sintering at this stage, generating massive new interlamellar 2D pores (Fig. 9(b)). Consequently, significantly faster sintering kinetics occur in both intrinsic interlamellar 2D pores and newly generated interlamellar 2D pores at stage I, as the sintering process of the ceramic is driven by a reduction in the free energy of the whole system. In Stage II, the interlamellar 2D pores with gap widths greater than the critical pore healing width are difficult to heal through multipoint contact (Fig. 9(c)). Therefore, matter transfer can proceed in only a single way, leading to significantly slower sintering kinetics.

The APS-RSZ coating consists of many splats and interlamellar 2D pores with two opposite surfaces formed by two splats across the pore. The changes in pore morphology, especially the roughness of the splat surface, significantly affect the sintering process of the interlamellar 2D pores.To further explore the critical width of the 2D pores in RSZ coating, we performed SEM (Figs. 10(a)–10(d)) and AFM (Figs. 10(e)–10(h)) surface scanning on an individual splat after different durations. The surface profiles (Figs. 10(i)–10(l)) obtained via AFM reveal that the splat surface transformed from flat to rough, which was accompanied by the rapid growth of the grains (Figs. 10(e)–10(h)), as confirmed by SEM surface scanning (Figs. 10(a)–10(d)). The cross-sectional profile (Fig. 10(i)–10(l)) shows that the surface roughness of a single splat tended to stabilize after thermal exposure for 10 h, with an increase in the surface height of less than 120 nm. Additionally, considering the variation in the critical pore healing width and multiplying the results by a coefficient of 1.2, the critical pore healing width in RSZ coating was estimated to be approximately 300–450 nm.

5.3.3 *Evidence of critical pore healing width*

To verify the existence of a critical pore healing width in APS-RSZ coating, we utilized 2D pore analysis method [112] to obtain the characteristic parameters of the intrinsic 2D pores and the newly generated 2D pores (Fig. 11). Although the formation mechanism of the newly generated 2D pores differs from that of the intrinsic 2D pores (Figs. 9(d) and 9(e)), the critical pore healing widths of these 2D pores can be expected to be similar because pore healing occurs via multipoint contact. The critical pore healing widths of the intrinsic 2D pores and the newly generated 2D pores are in the ranges of 300–400 and 400–500 nm, respectively (Figs. 11(b) and 11(e)). The critical pore healing width of the intrinsic 2D pores agrees with the value obtained on the basis of splat roughness. In addition, the residual 2D pore density of these 2D pores decreases with increasing thermal duration (Figs. 11(a) and 11(d)), and the pore aspect ratios gradually shift from > 90 to < 10 (Figs. 11(c) and 11(f)). These results are consistent with the conventional coating densification process [130] and are coupled with the thermal cycling results, suggesting that the proposed sintering-resistant coating design strategy is suitable for the fabrication of RSZ coatings with nanobimodal structures.

5.4 Investigation of the mechanism for lifespan enhancement

5.4.1 *Effects of stiffening changes on the stress and cracking driving force (SERR)*

We subjected RSZ coating to thermal exposure in a muffle furnace (SX-Q08163, Tianjin Zhonghuan Electric Furnace Co., Ltd., China) and used SEM-BSE to characterize the cross-sectional morphology under different heat treatment conditions. The thermal exposure temperature can affect the thermal history and, consequently, the mechanical properties of the coating. Two heat treatment temperatures, i.e., 1500 and 1050 °C, were used to evaluate the effects of temperature on the mechanical properties. As shown in Fig. 12(a), the elastic modulus of RSZ coating shows a typical two-stage increasing trend at both temperatures, reaching higher values at 1500 °C. Moreover, the elastic modulus of RSZ coating is lower than that of YSZ coating, regardless of the change

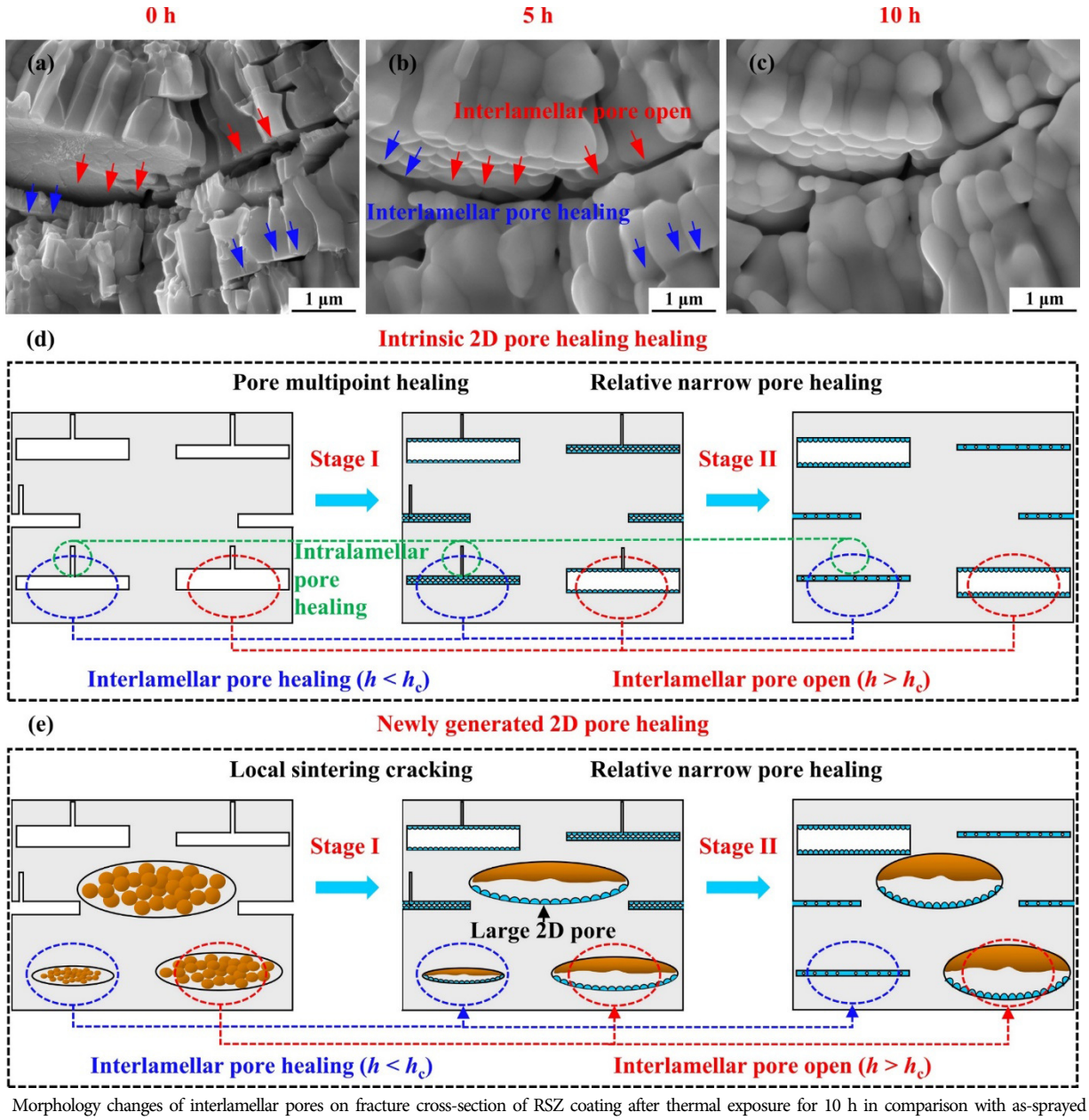

Fig. 9 Morphology changes of interlamellar pores on fracture cross-section of RSZ coating after thermal exposure for 10 h in comparison with as-sprayed RSZ: (a) as-sprayed coating; after thermal exposure for (b) 5 h and (c) 10 h. Schematic of evolution of (d) intrinsic 2D pores and (e) newly generated 2D pores with different widths.

in thermal duration (Fig. 12(b)). Generally, an increase in the elastic modulus is indicative of the degree of pore healing during sintering. Compared with YSZ coating, RSZ coating clearly has a lower degree of stiffening and higher sintering resistance during thermal exposure.

Our SEM observations (Fig. 8) and mechanical property characterization (Fig. 12) suggest that the sintering resistance of RSZ coating plays an important role in the thermal cycling failure of DL-TBCs. Because these characterizations were performed on samples subjected to thermal cycling tests, the stress distribution and evolution in the coating during thermal cycling remain unclear. Unfortunately, this process cannot be readily characterized via current experimental techniques. To understand the effect of sintering stiffening on the stress distribution and cracking driving force, we performed a thermal cycling simulation via ABAQUS 6.14 software (Fig. 13). During thermal cycling (from $N = 0$ cycle to $N = 200$ cycles), stress concentration occurs at the preexisting crack tip. The simulation data obtained for the tensile stress (σ_{22}) and shear stress (σ_{12}) (Figs. 14(a), 14(b), 14(d), and 14(e)) reveal that both σ_{22} and σ_{12} show a two-stage increase with increasing number of cycles, similar to the elastic modulus. This simulation result can be explained by the fact that, under thermal cycling, the sintering densification within the coating enhances the mechanical properties, especially the elastic modulus, which increases the stress concentration at the crack tip and the cracking driving force (Fig. 14(c)), thereby leading to an increased risk of coating spalling. It can be concluded that the microscopic pore structure regulation in RSZ coating enhances the sintering resistance by ensuring that RSZ coating and the bottom coating are tightly bonded, suggesting that lowering the stiffness induced during thermal cycling can reduce the cracking driving force and improve the thermal cycling lifespan.

5.4.2 Effect of thickness ratio on stress and cracking driving force (SERR)

In addition to sintering stiffening, the thickness ratio also alters the

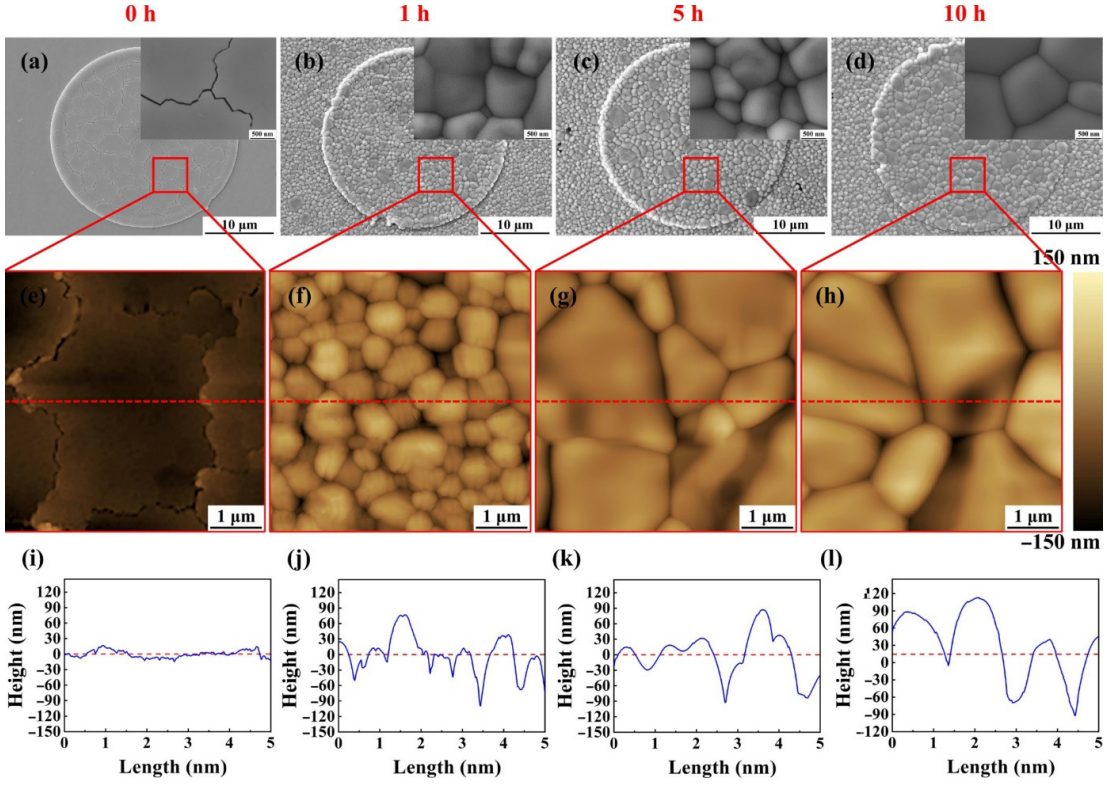

Fig. 10 Surface morphology and cross-sectional profiles of an individual RSZ splat at different states: (a) as-sprayed and after thermal exposure for (b) 1 h, (c) 5 h, and (d) 10 h. AFM surface morphology of an individual RSZ splat at typical different states: (e) as-sprayed and after thermal exposure for (f) 1 h, (g) 5 h, and (h) 10 h. Cross-sectional surface profiles of an individual RSZ splat over approximately the same region: (i) as-sprayed and after thermal exposure for (j) 1 h, (k) 5 h, and (l) 10 h.

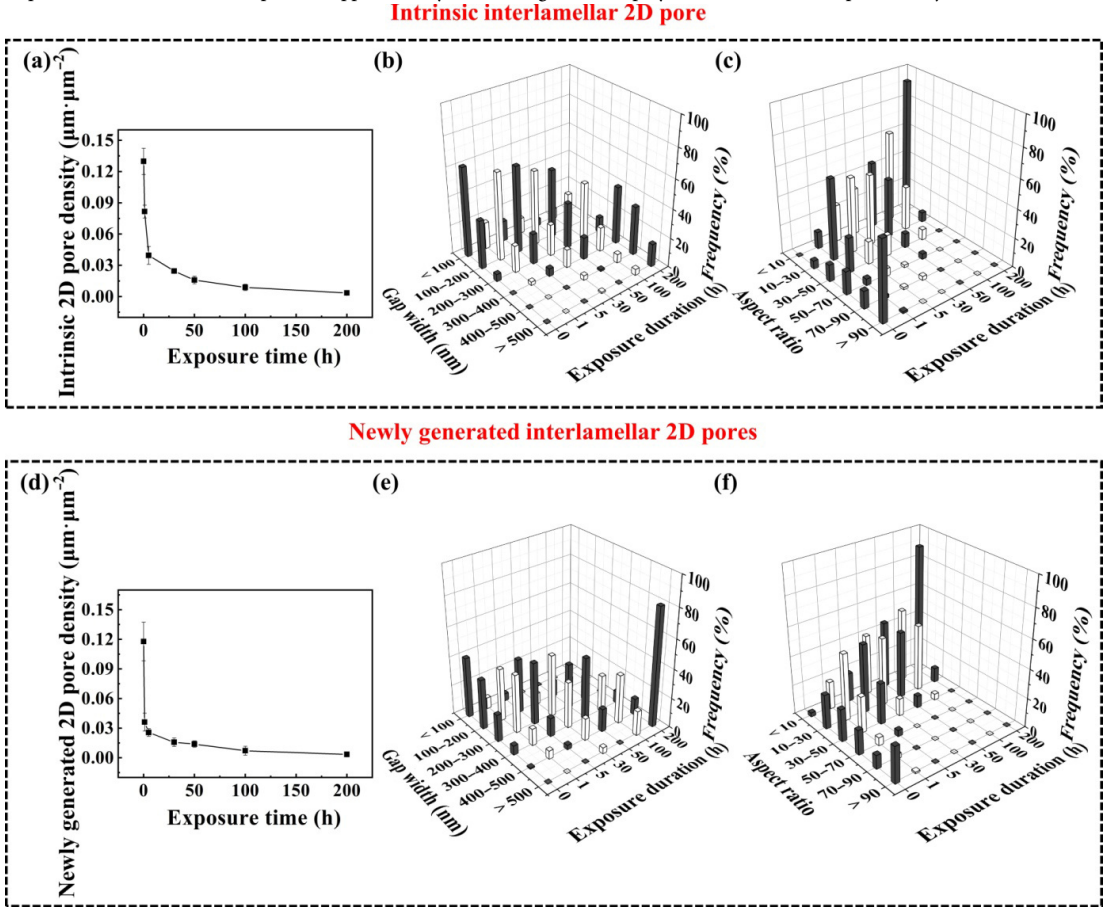

Fig. 11 Evolution during thermal exposure of intrinsic interlamellar 2D pores in terms of (a) residual 2D pore density, (b) width distribution, and (c) aspect ratio distribution. Evolution during thermal exposure of newly generated interlamellar 2D pores in terms of (d) residual 2D pore density, (e) width distribution, and (f) aspect ratio distribution.

https://doi.org/10.26599/JAC.2024.9221002

stress state in the coating. We performed a tension simulation with different thickness ratios using equivalent tensile strains (Fig. 15). σ_{22} and σ_{12} in the top cracking model relax rapidly when the crack interface moves upward continuously (the thickness ratio increases), whereas the stress in the bottom cracking model increases with the thickness ratio. The same trend was obtained for the SERR data via ABAQUS 6.14 (Fig. 16). This simulation result can be explained by the fact that the proportion of YSZ toughened layer increases with increasing thickness ratio, which effectively relieves the greater thermal mismatch stress between

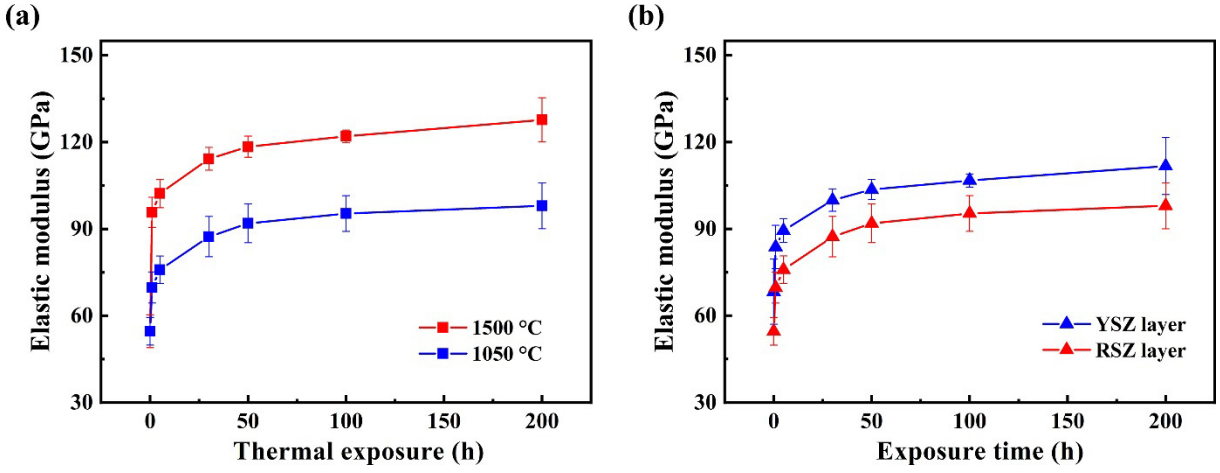

Fig. 12 Elastic modulus of (a) RSZ coating versus thermal duration at 1500 and 1050 °C, and (b) RSZ coating and YSZ coating versus thermal duration at 1050 °C.

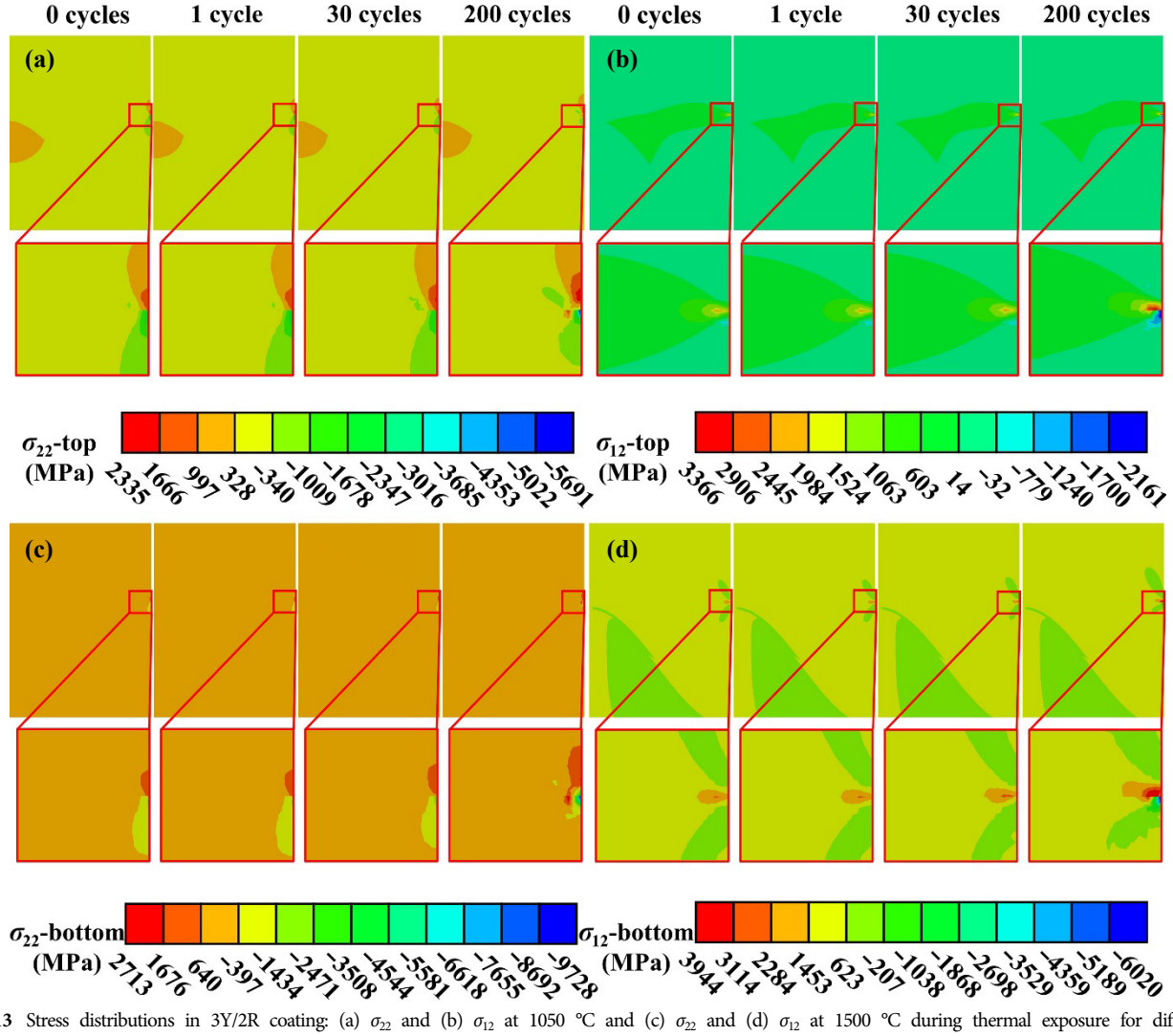

Fig. 13 Stress distributions in 3Y/2R coating: (a) σ_{22} and (b) σ_{12} at 1050 °C and (c) σ_{22} and (d) σ_{12} at 1500 °C during thermal exposure for different durations.

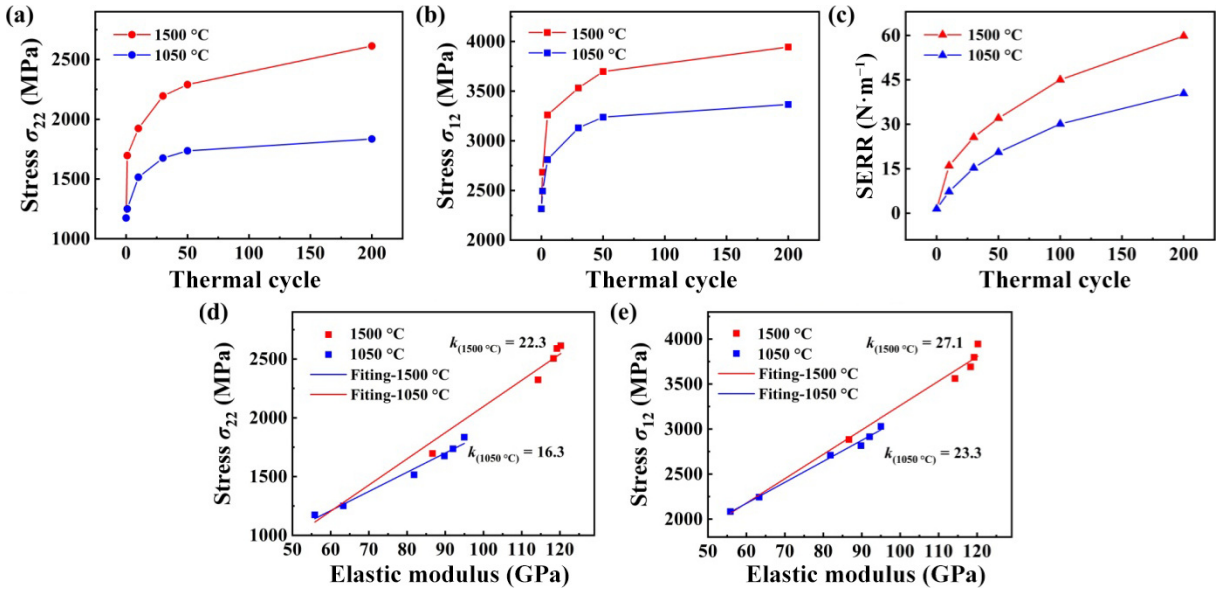

Fig. 14 Temperature-dependent residual stress at crack tip in 3Y/2R coating: (a, b) residual stress versus thermal cycles, (c) SERR versus thermal cycles, and (d, e) residual stress versus elastic modulus.

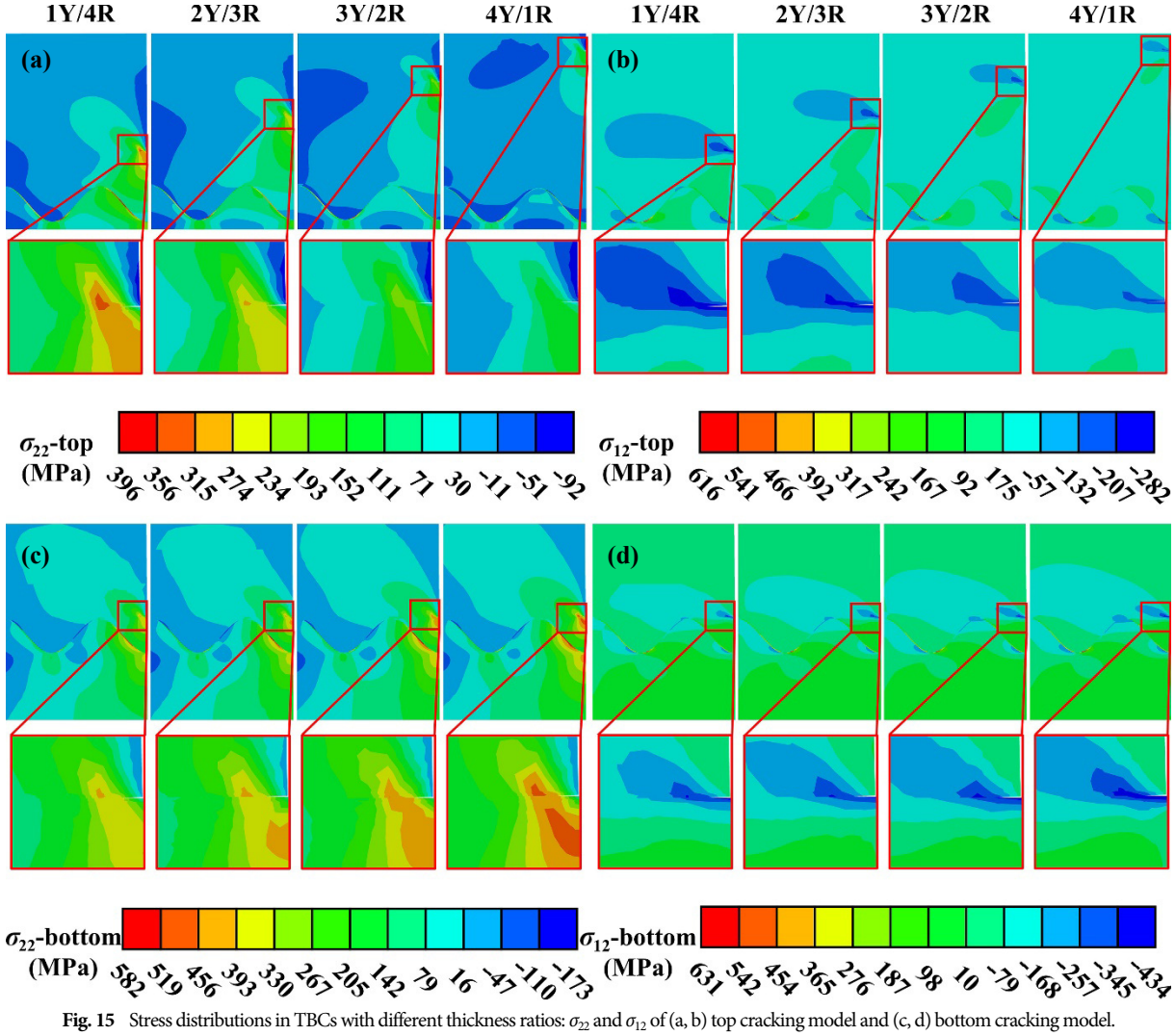

Fig. 15 Stress distributions in TBCs with different thickness ratios: σ_{22} and σ_{12} of (a, b) top cracking model and (c, d) bottom cracking model.

the RSZ layer and the bond layer, leading to a decrease in the SERR at the top cracking interface. The overall ceramic layer thickness increases with increasing thickness ratio, as does the SERR in the bottom cracking model, owing to the dominant role of the thickness.

The experimental and simulation results suggest that the

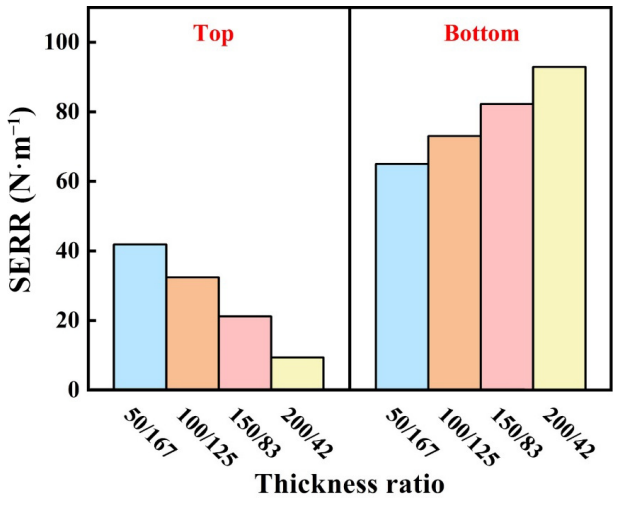

Fig. 16 SERR in top and bottom cracking models with different thickness ratios.

decreasing effect of RSZ layer fraction on SERR works in two ways: (i) The low-stiffness RSZ layer directly decreases SERR. (ii) The ceramic coating thickness decreases with increasing RSZ layer fraction, which also decreases the SERR. Therefore, under the prerequisite of ensuring that the RSZ layer and the bottom coating are tightly bonded, increasing the RSZ layer fraction maximally to reduce the cracking driving force is an effective way for improving the lifespan of the coating.

On the basis of the isothermal thermal cycling results of the six groups of YSZ/RSZ DL-TBCs, 3Y/2R TBCs with a thickness ratio of 150/83 have the longest lifespan of 690±10 cycles. Therefore, this thickness ratio was selected as the optimum thickness ratio for the equivalent thermal insulation design of 250 μm YSZ TBCs. 3Y/2R TBCs can withstand high temperatures up to 1500 °C. Moreover, these TBCs exhibit a lower cracking driving force and longer thermal cycling lifespan than the other three groups of DL-TBCs. 3Y/2R TBCs have strong thermal insulation capabilities, enabling the operation of the substrate at temperatures above 1300 °C. Moreover, tailoring the proportion and size of incompletely melted agglomerated nanoparticle stacks in the top ceramic layer is a way to achieve sintering resistance. Therefore, reducing the elastic modulus of the ceramic coating and inhibiting the growth of TGO at 3Y/2R can improve the thermal cycling lifespan of YSZ/RSZ DL-TBCs.

6 Conclusions

In this study, the lifespan of TBCs was increased by designing a thermal insulation structure based on agglomerated nanoparticle stacks. The underlying mechanisms responsible for the long lifespan were investigated. The detailed conclusions are as follows:

1) Durable DL-TBCs with multiscale structures under equivalent thermal insulation were prepared. TBCs with the optimized thickness ratio (2:3) presented approximately two and nineteen times longer lifespans than the conventional YSZ and RSZ samples, respectively.

2) The lamellar cracking within the ceramic coating was the main reason for the failure of all TBCs. With decreasing RSZ proportion, the failure mode changed from spallation of the top layer to delamination of the double-layered structure.

3) An analysis of the pore structure evolution in different regions was conducted via AFM technique to demonstrate the failure behavior. Healing of the intrinsic 2D pores and the formation of newly generated lamellar pores play a dominant role in the changes in the thermal and mechanical properties.

4) The load-bearing conditions during thermal exposure were investigated via simulation. The multiscale design reduced SERR due to higher sintering resistance and optimized thinner thickness, which can be responsible for the long lifespan.

Acknowledgements

This work was supported by the National Natural Science Foundation of China (No. 52371075), the National Training Program of Innovation and Entrepreneurship for Undergraduates, the Young Elite Scientists Sponsorship Program by CAST (No. YESS20200083), the Young Talent Fund of the University Association for Science and Technology in Shaanxi, China (No. 20190403), and the Fundamental Research Funds for the Central Universities (No. xzy012022057).

Declaration of competing interest

The authors have no competing interests to declare that are relevant to the content of this article. The author Guan-Jun Yang is the Editorial Committee member of this journal.

References

[1] Perepezko JH. The hotter the engine, the better. *Science* 2009, **326**: 1068–1069.

[2] Clarke DR, Oechsner M, Padture NP. Thermal-barrier coatings for more efficient gas-turbine engines. *MRS Bull* 2012, **37**: 891–898.

[3] Wang J, Jin QQ, Song JB, *et al.* Revealing the low thermal conductivity of high-entropy rare-earth tantalates via multi-scale defect analysis. *J Adv Ceram* 2023, **12**: 2087–2100.

[4] Cong LK, Li W, Wang JC, *et al.* High-entropy $(Y_{0.2}Gd_{0.2}Dy_{0.2}Er_{0.2}Yb_{0.2})_2Hf_2O_7$ ceramic: A promising thermal barrier coating material. *J Mater Sci Technol* 2022, **101**: 199–204.

[5] Cai HY, Shan X, Lu J, *et al.* The crack behavior and delamination mechanisms of air plasma sprayed thermal barrier coatings under ultrasonic plasma jet at 1600 °C. *J Eur Ceram Soc* 2023, **43**: 4136–4145.

[6] Han Y, Zong PA, Huang MZ, *et al. In-situ* synthesis of gadolinium niobate quasi-binary composites with balanced mechanical and thermal properties for thermal barrier coatings. *J Adv Ceram* 2022, **11**: 1445–1456.

[7] Chen L, Li BH, Guo J, *et al.* High-entropy perovskite $RETa_3O_9$ ceramics for high-temperature environmental/thermal barrier coatings. *J Adv Ceram* 2022, **11**: 556–569.

[8] Xue Y, Zhao XQ, An YL, *et al.* High-entropy $(La_{0.2}Nd_{0.2}Sm_{0.2}Eu_{0.2}Gd_{0.2})_2Ce_2O_7$: A potential thermal barrier material with improved thermo-physical properties. *J Adv Ceram* 2022, **11**: 615–628.

[9] Guo L, Li BW, Cheng YX, *et al.* Composition optimization, high-temperature stability, and thermal cycling performance of Sc-doped $Gd_2Zr_2O_7$ thermal barrier coatings: Theoretical and experimental studies. *J Adv Ceram* 2022, **11**: 454–469.

[10] Hu DY, Lv ZZ, Liu HY, *et al.* Characterization and mechanical modeling of interfacial damage in EB-PVD thermal barrier coatings considering multiple failure factors. *J Mater Sci Technol* 2024, **190**: 42–55.

[11] Sang WW, Zhang HS, Liu SX, *et al.* Thermophysical performances of Sm_2O_3-doped Gd_3TaO_7 oxides for thermal barrier coatings. *J Eur Ceram Soc* 2023, **43**: 3676–3683.

[12] Stopyra M, Moskal G, Mikuśkiewicz M, *et al.* A new concept of the chemical composition design of ultra-low conducting thermal barrier coatings. *J Eur Ceram Soc* 2024, **44**: 5129–5137.

[13] Gan MD, Lu TL, Yu W, *et al.* Capturing and visualizing the phase transition mediated thermal stress of thermal barrier coating materials via a cross-scale integrated computational approach. *J Adv Ceram* 2024, **13**: 413–428.

[14] Li P, Jin XC, Lu P, *et al.* Comparative study on microstructure

evolution and failure mechanisms of ordinary and refurbished EB-PVD TBC under cyclic oxidation. *J Adv Ceram* 2023, **12**: 1805–1820.
[15] Wei ZY, Meng GH, Chen L, *et al.* Progress in ceramic materials and structure design toward advanced thermal barrier coatings. *J Adv Ceram* 2022, **11**: 985–1068.
[16] Liu SH, Ji G, Li CJ, *et al.* Novel long laminar plasma sprayed hybrid structure thermal barrier coatings for high-temperature anti-sintering and volcanic ash corrosion resistance. *J Mater Sci Technol* 2021, **79**: 141–146.
[17] Chen HY, Yan JJ, Cao K, *et al.* Friction delamination mechanism of EB-PVD thermal barrier coatings in high-temperature and high-speed rotating service environment. *J Eur Ceram Soc* 2023, **43**: 3637–3646.
[18] Zhang ZJ, Sun J, Liu GH, *et al.* High toughness and CMAS resistance of $REAlO_3/RE_2Zr_2O_7$ (RE = La, Nd, Sm, Eu, Gd, and Dy) composites with eutectic composition for thermal barrier coatings. *J Adv Ceram* 2024, **13**: 800–809.
[19] Trice RW, Su YJ, Mawdsley JR, *et al.* Effect of heat treatment on phase stability, microstructure, and thermal conductivity of plasma-sprayed YSZ. *J Mater Sci* 2002, **37**: 2359–2365.
[20] Ilavsky J, Stalick JK. Phase composition and its changes during annealing of plasma-sprayed YSZ. *Surf Coat Tech* 2000, **127**: 120–129.
[21] Vogt T, Hunter BA, Thornton J. Structural evolution of thermal-sprayed yttria-stabilized ZrO_2 thermal barrier coatings with annealing—A neutron diffraction study. *J Am Ceram Soc* 2001, **84**: 678–680.
[22] Yang GJ, Chen ZL, Li CX, *et al.* Microstructural and mechanical property evolutions of plasma-sprayed YSZ coating during high-temperature exposure: Comparison study between 8YSZ and 20YSZ. *J Therm Spray Techn* 2013, **22**: 1294–1302.
[23] Li GR, Xie H, Yang GJ. Scale-progressive healing mechanism dominating the ultrafast initial sintering kinetics of plasma-sprayed thermal barrier coatings. *Ceram Int* 2018, **44**: 16732–16738.
[24] Li GR, Yang GJ, Li CX, *et al.* A comprehensive mechanism for the sintering of plasma-sprayed nanostructured thermal barrier coatings. *Ceram Int* 2017, **43**: 9600–9615.
[25] Wang LS, Song JB, Dong H, *et al.* Sintering-induced failure mechanism of thermal barrier coatings and sintering-resistant design. *Coatings* 2022, **12**: 1083.
[26] Lv BW, Wang C, Zhang XF, *et al.* Stress-dependent sintering behavior of porous thermal barrier coatings. *J Eur Ceram Soc* 2023, **43**: 2634–2645.
[27] Paul S, Cipitria A, Golosnoy IO, *et al.* Effects of impurity content on the sintering characteristics of plasma-sprayed zirconia. *J Therm Spray Techn* 2007, **16**: 798–803.
[28] Cernuschi F, Lorenzoni L, Ahmaniemi S, *et al.* Studies of the sintering kinetics of thick thermal barrier coatings by thermal diffusivity measurements. *J Eur Ceram Soc* 2005, **25**: 393–400.
[29] Li GR, Yang GJ. Understanding of degradation-resistant behavior of nanostructured thermal barrier coatings with bimodal structure. *J Mater Sci Technol* 2019, **35**: 231–238.
[30] Wei ZY, Cai HN, Li CJ. Comprehensive dynamic failure mechanism of thermal barrier coatings based on a novel crack propagation and TGO growth coupling model. *Ceram Int* 2018, **44**: 22556–22566.
[31] Zhu DM, Miller RA. Development of advanced low conductivity thermal barrier coatings. *Int J Appl Ceram Tec* 2004, **1**: 86–94.
[32] Ball JAJ, Martins JF, Brewster G, *et al.* An investigation into RESZ (RE = Yb, Er, Gd, Sm) materials for CMAS resistance in thermal barrier coatings. *J Eur Ceram Soc* 2024, **44**: 3734–3746.
[33] Liu DB, Shi BL, Geng LY, *et al.* High-entropy rare-earth zirconate ceramics with low thermal conductivity for advanced thermal-barrier coatings. *J Adv Ceram* 2022, **11**: 961–973.
[34] Tu TZ, Liu JX, Wu Y, *et al.* Synergistic effects of high-entropy engineering and particulate toughening on the properties of rare-earth aluminate-based ceramic composites. *J Adv Ceram* 2023, **12**: 861–872.
[35] Zhong Y, Liu Y, Jiang QK, *et al.* Improvement of mechanical properties and investigation of strengthening mechanisms on the Ti_3AlC_2 ceramic with nanosized WC addition. *J Adv Ceram* 2024, **13**: 861–876.
[36] Li CY, Gao RN, Ouyang HB, *et al.* Hierarchical porous $(Ta_{0.2}Nb_{0.2}Ti_{0.2}Zr_{0.2}Hf_{0.2})C$ high-entropy ceramics prepared by a self-foaming method for thermal insulation. *J Adv Ceram* 2024, **13**: 956–966.
[37] Zhang S, Wang XH, Zhang C, *et al.* Microstructure, elastic/mechanical and thermal properties of $CrTaO_4$: A new thermal barrier material. *J Adv Ceram* 2024, **13**: 373–387.
[38] Karabaş M, Bal E, Taptık Y. Thermal cycling behavior of $La_2Zr_2O_7$ thermal barrier coatings by plasma spraying of an amorphous and crystalline precursors. *Mater Res Express* 2018, **6**: 015514.
[39] Karabaş M. Production and characterization of Nd and Dy doped lanthanum zirconate-based thermal barrier coatings. *Surf Coat Tech* 2020, **394**: 125864.
[40] Yu HY, Shi YY, Shi MC, *et al.* High-temperature sintering behavior of Gd_2O_3–Yb_2O_3 co-doped 8YSZ ceramic for thermal barrier coatings. *J Mater Eng Perform* 2024, **33**: 1588–1595.
[41] Gao PH, Zeng SC, Jin C, *et al.* Effect of Gd_2O_3 addition on the microstructure and properties of Gd_2O_3–Yb_2O_3–Y_2O_3–ZrO_2 (GYYZO) ceramics. *Materials* 2021, **14**: 7470.
[42] Qian G, Nakamura T, Berndt CC, *et al.* Tensile toughness test and high temperature fracture analysis of thermal barrier coatings. *Acta Mater* 1997, **45**: 1767–1784.
[43] Vassen R, Cao XQ, Tietz F, *et al.* Zirconates as new materials for thermal barrier coatings. *J Am Ceram Soc* 2000, **83**: 2023–2028.
[44] Dwivedi G, Viswanathan V, Sampath S, *et al.* Fracture toughness of plasma-sprayed thermal barrier ceramics: Influence of processing, microstructure, and thermal aging. *J Am Ceram Soc* 2014, **97**: 2736–2744.
[45] Liu B, Liu YC, Zhu CH, *et al.* Advances on strategies for searching for next generation thermal barrier coating materials. *J Mater Sci Technol* 2019, **35**: 833–851.
[46] Stöver D, Pracht G, Lehmann H, *et al.* New material concepts for the next generation of plasma-sprayed thermal barrier coatings. *J Therm Spray Techn* 2004, **13**: 76–83.
[47] Wang XY, Guo SN, Zhao LL, *et al.* A novel thermal barrier coating for high-temperature applications. *Ceram Int* 2016, **42**: 2648–2653.
[48] Huang JB, Wang WZ, Li YJ, *et al.* Novel-structured plasma-sprayed thermal barrier coatings with low thermal conductivity, high sintering resistance and high durability. *Ceram Int* 2021, **47**: 5156–5167.
[49] Wang JS, Sun JB, Jing QS, *et al.* Phase stability and thermo-physical properties of ZrO_2–CeO_2–TiO_2 ceramics for thermal barrier coatings. *J Eur Ceram Soc* 2018, **38**: 2841–2850.
[50] Tsipas SA. Effect of dopants on the phase stability of zirconia-based plasma sprayed thermal barrier coatings. *J Eur Ceram Soc* 2010, **30**: 61–72.
[51] Krogstad JA, Krämer S, Lipkin DM, *et al.* Phase stability of *t*′-zirconia-based thermal barrier coatings: Mechanistic insights. *J Am Ceram Soc* 2011, **94**: s168–s177.
[52] Doleker KM, Karaoglanli AC, Ozgurluk Y, *et al.* Performance of single YSZ, $Gd_2Zr_2O_7$ and double-layered YSZ/$Gd_2Zr_2O_7$ thermal barrier coatings in isothermal oxidation test conditions. *Vacuum* 2020, **177**: 109401.
[53] Ma XQ, Rivellini K, Ruggiero P, *et al.* Toward durable thermal barrier coating with composite phases and low thermal conductivity. *J Therm Spray Techn* 2020, **29**: 423–432.
[54] Van Sluytman JS, Krämer S, Tolpygo VK, *et al.* Microstructure evolution of ZrO_2–$YbTaO_4$ thermal barrier coatings. *Acta Mater* 2015, **96**: 133–142.
[55] Liu L, Dong HY, Zhang P, *et al.* Design and experimental investigation of potential low-thermal-conductivity high-entropy rare-earth zirconates. *J Adv Ceram* 2024, **13**: 1132–1142.
[56] Zhu JT, Wei MY, Xu J, *et al.* Influence of order–disorder transition

on the mechanical and thermophysical properties of $A_2B_2O_7$ high-entropy ceramics. *J Adv Ceram* 2022, **11**: 1222–1234.
[57] Tan ZY, Yang ZH, Zhu W, *et al.* Mechanical properties and calcium–magnesium–alumino–silicate (CMAS) corrosion behavior of a promising $Hf_6Ta_2O_{17}$ ceramic for thermal barrier coatings. *Ceram Int* 2020, **46**: 25242–25248.
[58] Li WS, Zhao HY, Zhong XH, *et al.* Air plasma-sprayed yttria and yttria-stabilized zirconia thermal barrier coatings subjected to calcium–magnesium–alumino–silicate (CMAS). *J Therm Spray Techn* 2014, **23**: 975–983.
[59] Li Y, She YJ, Liao K. Hot-corrosion behavior of Gd_2O_3–Yb_2O_3 co-doped YSZ thermal barrier coatings in the presence of V_2O_5 molten salt. *Coatings* 2023, **13**: 886.
[60] Tian ZL, Ming KY, Zheng LY, *et al. In-situ* observation and mechanism of calcium–magnesium–alumina–silicate (CMAS) melts-induced degradation of RE_2SiO_5 (RE = Tb, Dy, Ho, Y, Er, Tm, and Yb) ceramics at 1500 °C. *J Adv Ceram* 2023, **12**: 2315–2330.
[61] Guo L, Li YY, Li G. Design of Ti_2AlC/YSZ TBCs for more efficient in resisting CMAS attack. *J Adv Ceram* 2023, **12**: 1712–1730.
[62] Bal E, Karabaş M. Effect of molten glass on degradation of stabilized zirconia thermal barrier coatings. *J Korean Ceram Soc* 2023, **60**: 331–343.
[63] Odabas O, Ozgurluk Y, Ozkan D, *et al.* Investigation of vermiculite infiltration effect on microstructural properties of thermal barrier coatings (TBCs) produced by electron beam physical vapor deposition method (EB-PVD). *Surf Coat Tech* 2022, **443**: 128645.
[64] Ozgurluk Y, Karaoglanli AC, Ahlatci H. Comparison of calcium–magnesium–alumina–silicate (CMAS) resistance behavior of produced with electron beam physical vapor deposition (EB-PVD) method YSZ and $Gd_2Zr_2O_7$/YSZ thermal barrier coatings systems. *Vacuum* 2021, **194**: 110576.
[65] Ozgurluk Y, Doleker KM, Ahlatci H, *et al.* Investigation of calcium–magnesium–alumino–silicate (CMAS) resistance and hot corrosion behavior of YSZ and $La_2Zr_2O_7$/YSZ thermal barrier coatings (TBCs) produced with CGDS method. *Surf Coat Tech* 2021, **411**: 126969.
[66] Doleker KM, Ozgurluk Y, Kahraman Y, *et al.* Oxidation and hot corrosion resistance of HVOF/EB-PVD thermal barrier coating system. *Surf Coat Tech* 2021, **409**: 126862.
[67] Ozgurluk Y, Doleker KM, Karaoglanli AC. Hot corrosion behavior of YSZ, $Gd_2Zr_2O_7$ and YSZ/$Gd_2Zr_2O_7$ thermal barrier coatings exposed to molten sulfate and vanadate salt. *Appl Surf Sci* 2018, **438**: 96–113.
[68] Kirbiyik F, Gok MG, Goller G. Application of thermal gradient and thermal cycling tests to Al_2O_3/CYSZ functionally graded TBC in the presence of simultaneous hot corrosion and CMAS effects. *Surf Coat Tech* 2022, **444**: 128688.
[69] Xie XY, Guo HB, Gong SK, *et al.* Lanthanum–titanium–aluminum oxide: A novel thermal barrier coating material for applications at 1300 °C. *J Eur Ceram Soc* 2011, **31**: 1677–1683.
[70] Wang Y, Guo HB, Gong SK. Thermal shock resistance and mechanical properties of $La_2Ce_2O_7$ thermal barrier coatings with segmented structure. *Ceram Int* 2009, **35**: 2639–2644.
[71] Zhang DB, Zhao ZY, Wang BY, *et al.* Investigation of a new type of composite ceramics for thermal barrier coatings. *Mater Design* 2016, **112**: 27–33.
[72] Wang J, Bai SX, Zhang H, *et al.* The structure, thermal expansion coefficient and sintering behavior of Nd^{3+}-doped $La_2Zr_2O_7$ for thermal barrier coatings. *J Alloys Compd* 2009, **476**: 89–91.
[73] Pakseresht A, Sharifianjazi F, Esmaeilkhanian A, *et al.* Failure mechanisms and structure tailoring of YSZ and new candidates for thermal barrier coatings: A systematic review. *Mater Design* 2022, **222**: 111044.
[74] Mehboob G, Liu MJ, Xu T, *et al.* A review on failure mechanism of thermal barrier coatings and strategies to extend their lifetime. *Ceram Int* 2020, **46**: 8497–8521.
[75] Song JB, Wang LS, Dong H, *et al.* Long lifespan thermal barrier coatings overview: Materials, manufacturing, failure mechanisms, and multiscale structural design. *Ceram Int* 2023, **49**: 1–23.
[76] Karaoglanli AC, Doleker KM, Ozgurluk Y. Interface failure behavior of yttria stabilized zirconia (YSZ), $La_2Zr_2O_7$, $Gd_2Zr_2O_7$, YSZ/$La_2Zr_2O_7$ and YSZ/$Gd_2Zr_2O_7$ thermal barrier coatings (TBCs) in thermal cyclic exposure. *Mater Charact* 2020, **159**: 110072.
[77] Vaßen R, Bakan E, Mack DE, *et al.* A perspective on thermally sprayed thermal barrier coatings: Current status and trends. *J Therm Spray Techn* 2022, **31**: 685–698.
[78] Doleker KM, Ozgurluk Y, Karaoglanli AC. TGO growth and kinetic study of single and double layered TBC systems. *Surf Coat Tech* 2021, **415**: 127135.
[79] Dong H, Yang GJ, Li CX, *et al.* Effect of TGO thickness on thermal cyclic lifetime and failure mode of plasma-sprayed TBCs. *J Am Ceram Soc* 2014, **97**: 1226–1232.
[80] Aktaa J, Sfar K, Munz D. Assessment of TBC systems failure mechanisms using a fracture mechanics approach. *Acta Mater* 2005, **53**: 4399–4413.
[81] Li CJ, Dong H, Ding H, *et al.* The correlation of the TBC lifetimes in burner cycling test with thermal gradient and furnace isothermal cycling test by TGO effects. *J Therm Spray Techn* 2017, **26**: 378–387.
[82] Cao XQ, Vassen R, Tietz F, *et al.* New double-ceramic-layer thermal barrier coatings based on zirconia–rare earth composite oxides. *J Eur Ceram Soc* 2006, **26**: 247–251.
[83] Viswanathan V, Dwivedi G, Sampath S. Engineered multilayer thermal barrier coatings for enhanced durability and functional performance. *J Am Ceram Soc* 2014, **97**: 2770–2778.
[84] Chen XL, Zhao Y, Fan XZ, *et al.* Thermal cycling failure of new $LaMgAl_{11}O_{19}$/YSZ double ceramic top coat thermal barrier coating systems. *Surf Coat Tech* 2011, **205**: 3293–3300.
[85] Zhang H, Yuan JY, Song WJ, *et al.* Composition, mechanical properties and thermal cycling performance of YSZ toughened $La_2Ce_2O_7$ composite thermal barrier coatings. *Ceram Int* 2020, **46**: 6641–6651.
[86] Vaßen R, Bakan E, Mack D, *et al.* Performance of YSZ and $Gd_2Zr_2O_7$/YSZ double layer thermal barrier coatings in burner rig tests. *J Eur Ceram Soc* 2020, **40**: 480–490.
[87] Doleker KM, Ozgurluk Y, Ahlatci H, *et al.* Evaluation of oxidation and thermal cyclic behavior of YSZ, $Gd_2Zr_2O_7$, and YSZ/$Gd_2Zr_2O_7$ TBCs. *Surf Coat Tech* 2019, **371**: 262–275.
[88] Doleker KM, Ozgurluk Y, Karaoglanli AC. Isothermal oxidation and thermal cyclic behaviors of YSZ and double-layered YSZ/$La_2Zr_2O_7$ thermal barrier coatings (TBCs). *Surf Coat Tech* 2018, **351**: 78–88.
[89] Gok MG, Goller G. Production and characterisation of GZ/CYSZ alternative thermal barrier coatings with multilayered and functionally graded designs. *J Eur Ceram Soc* 2016, **36**: 1755–1764.
[90] Chen Q, Hu P, Pu J, *et al.* Sensitivity analysis and multi-objective optimization of double-ceramic-layers thermal barrier system. *Ceram Int* 2019, **45**: 17224–17235.
[91] Xu R, Fan XL, Wang TJ. Mechanisms governing the interfacial delamination of thermal barrier coating system with double ceramic layers. *Appl Surf Sci* 2016, **370**: 394–402.
[92] Liu Q, Hu XP, Zhu W, *et al.* Thermal shock performance and failure behavior of $Zr_6Ta_2O_{17}$–8YSZ double-ceramic-layer thermal barrier coatings prepared by atmospheric plasma spraying. *Ceram Int* 2022, **48**: 24402–24410.
[93] Dai H, Zhong XH, Li JY, *et al.* Thermal stability of double-ceramic-layer thermal barrier coatings with various coating thickness. *Mater Sci Eng A* 2006, **433**: 1–7.
[94] Liu K, Bai Y, Li JR, *et al.* Structure–property relationship and design of plasma-sprayed $La_2Ce_2O_7$/8YSZ composite coatings for gas turbine blades. *Ceram Int* 2018, **44**: 13662–13673.
[95] Mahade S, Curry N, Jonnalagadda KP, *et al.* Influence of YSZ layer thickness on the durability of gadolinium zirconate/YSZ double-layered thermal barrier coatings produced by suspension plasma spray. *Surf Coat Tech* 2019, **357**: 456–465.
[96] Zhu YQ, Yan B, Deng M, *et al.* Surrogate model for energy release rate and structure optimization of double-ceramic-layers thermal barrier coatings system. *Surf Coat Tech* 2022, **430**: 127989.

[97] Vaßen R, Jarligo MO, Steinke T, *et al.* Overview on advanced thermal barrier coatings. *Surf Coat Tech* 2010, **205**: 938–942.
[98] Cheng B, Yang GJ, Zhang Q, *et al.* Gradient thermal cyclic behaviour of $La_2Zr_2O_7$/YSZ DCL-TBCs with equivalent thermal insulation performance. *J Eur Ceram Soc* 2018, **38**: 1888–1896.
[99] Cheng B, Wei ZY, Chen L, *et al.* Prolong the durability of $La_2Zr_2O_7$/YSZ TBCs by decreasing the cracking driving force in ceramic coatings. *J Eur Ceram Soc* 2018, **38**: 5482–5488.
[100] Wei ZY, Cheng B, Wang J, *et al.* Extend the thermal cyclic lifetime of $La_2Zr_2O_7$/YSZ DCL TBCs by reducing modulus design on a toughening ceramic surface. *Surf Coat Tech* 2019, **374**: 134–143.
[101] Liu GX, Shen ZY, He LM, *et al.* LaYZrO/YSZ double ceramic layer thermal barrier coatings by EB-PVD: Thermal performance, morphology and failure behavior. *Materialia* 2023, **27**: 101661.
[102] Shen ZY, He LM, Mu RD, *et al.* Effects of gradient transitional layer on thermal cycling life and failure of LaZrCeO/YSZ thermal barrier coatings. *Corros Sci* 2020, **163**: 108224.
[103] Han JS, Zou Y, Wu DT, *et al.* Investigating the thermal, mechanical and thermal cyclic properties of plasma-sprayed Al_2O_3–7YSZ/7YSZ double ceramic layer TBCs. *J Eur Ceram Soc* 2023, **43**: 4124–4135.
[104] Yan G, Sun Y, Zhao XL, *et al.* The enhanced thermal shock resistance performance induced by interface effect in blade-level $La_2Ce_2O_7$/YSZ thermal barrier coating. *Appl Surf Sci* 2023, **619**: 156723.
[105] Shen ZY, Liu GX, Luo YQ, *et al.* Thermal property and failure behaviour of Pr doped $Gd_2Zr_2O_7$ thermal barrier coatings. *Corros Sci* 2024, **226**: 111641.
[106] Wu MM, Liu Y, Qu WW, *et al.* Thickness-related failure behaviors of the thermal barrier coatings under thermal gradient cycling. *Surf Coat Tech* 2023, **468**: 129748.
[107] Han M, Zhou GD, Huang JH, *et al.* A parametric study of the double-ceramic-layer thermal barrier coatings part I: Optimization design of the ceramic layer thickness ratio based on the finite element analysis of thermal insulation (take LZ_7C_3/8YSZ/NiCoAlY DCL-TBC for an example). *Surf Coat Tech* 2013, **236**: 500–509.
[108] Praveen K, Shanmugavelayutham G, Rao DS, *et al.* Thermal cycling performance assessment of double-layered lanthanum titanium aluminate thermal barrier coatings developed using plasma spheroidized powders. *Surf Coat Tech* 2023, **465**: 129588.
[109] Yang T, Wang WZ, Tang ZX, *et al.* Structural optimization for porous thermal barrier coating and analysis of thermomechanical properties by experimental and computational investigation. *Surf Coat Tech* 2023, **458**: 129347.
[110] Ponnapureddy S, Bhadauria A, Bajpai S, *et al.* Enhanced reliability with bimodal microstructure and transformation-induced toughening in Al_2O_3–YSZ based thermal barrier coatings. *Surf Coat Tech* 2023, **462**: 129488.
[111] Zhang WW, Li GR, Zhang Q, *et al.* Self-enhancing thermal insulation performance of bimodal-structured thermal barrier coating. *J Therm Spray Techn* 2018, **27**: 1064–1075.
[112] Li CJ, Wang WZ. Quantitative characterization of lamellar microstructure of plasma-sprayed ceramic coatings through visualization of void distribution. *Mater Sci Eng A* 2004, **386**: 10–19.
[113] Li CJ, Ohmori A, McPherson R. The relationship between microstructure and Young's modulus of thermally sprayed ceramic coatings. *J Mater Sci* 1997, **32**: 997–1004.
[114] Li CJ, Ohmori A. Relationships between the microstructure and properties of thermally sprayed deposits. *J Therm Spray Techn* 2002, **11**: 365–374.
[115] McPherson R. A review of microstructure and properties of plasma sprayed ceramic coatings. *Surf Coat Tech* 1989, **39–40**: 173–181.
[116] Thompson JA, Clyne TW. The effect of heat treatment on the stiffness of zirconia top coats in plasma-sprayed TBCs. *Acta Mater* 2001, **49**: 1565–1575.
[117] Dutton R, Wheeler R, Ravichandran KS, *et al.* Effect of heat treatment on the thermal conductivity of plasma-sprayed thermal barrier coatings. *J Therm Spray Techn* 2000, **9**: 204–209.
[118] Curry N, Janikowski W, Pala Z, *et al.* Impact of impurity content on the sintering resistance and phase stability of dysprosia- and yttria-stabilized zirconia thermal barrier coatings. *J Therm Spray Techn* 2014, **23**: 160–169.
[119] Zhang WW, Li GR, Zhang Q, *et al.* Comprehensive damage evaluation of localized spallation of thermal barrier coatings. *J Adv Ceram* 2017, **6**: 230–239.
[120] Li GR, Yang GJ, Li CX, *et al.* Strain-induced multiscale structural changes in lamellar thermal barrier coatings. *Ceram Int* 2017, **43**: 2252–2266.
[121] Zhang YL, Guo L, Yang YP, *et al.* Influence of Gd_2O_3 and Yb_2O_3 co-doping on phase stability, thermo-physical properties and sintering of 8YSZ. *Chinese J Aeronaut* 2012, **25**: 948–953.
[122] Guo L, Li MZ, Ye FX. Phase stability and thermal conductivity of re_2o_3 (RE = La, Nd, Gd, Yb) and Yb_2O_3 co-doped Y_2O_3 stabilized ZrO_2 ceramics. *Ceram Int* 2016, **42**: 7360–7365.
[123] Bobzin K, Zhao LD, Öte M, *et al.* A highly porous thermal barrier coating based on Gd_2O_3–Yb_2O_3 co-doped YSZ. *Surf Coat Tech* 2019, **366**: 349–354.
[124] Zhang YH, Sun YN, Tan X, *et al.* High temperature stability and sintering resistance of Gd_2O_3–Yb_2O_3–Y_2O_3–ZrO_2 (GYYZO) coating. *Surf Coat Tech* 2023, **459**: 129405.
[125] Chi W, Sampath S, Wang H. Microstructure–thermal conductivity relationships for plasma-sprayed yttria-stabilized zirconia coatings. *J Am Ceram Soc* 2008, **91**: 2636–2645.
[126] Li CJ, Li Y, Yang GJ, *et al.* A novel plasma-sprayed durable thermal barrier coating with a well-bonded YSZ interlayer between porous YSZ and bond coat. *J Therm Spray Techn* 2012, **21**: 383–390.
[127] Negami M, Yamabe-Mitarai Y. The oxidation behaviors of NiCoCrAlY coatings after pre-oxidation treatment during high-temperature oxidation at 800 °C and 900 °C. *High Temp Corros Mater* 2024, **101**: 511–527.
[128] Tang JJ, Bai Y, Wang JW, *et al.* Preheating treatment of thermal barrier coatings by supersonic plasma jet. *Mater Lett* 2016, **182**: 181–184.
[129] Li GR, Liu T, Luo XT, *et al.* Tailoring sintering-resistant thermal barrier coatings by considering critical healing width of two-dimensional interlamellar pores. *J Adv Ceram* 2023, **12**: 1317–1330.
[130] Liu T, Luo XT, Chen X, *et al.* Morphology and size evolution of interlamellar two-dimensional pores in plasma-sprayed $La_2Zr_2O_7$ coatings during thermal exposure at 1300 °C. *J Therm Spray Techn* 2015, **24**: 739–748.
[131] Cheruvu NS, Chan KS, Gandy DW. Effect of time and temperature on thermal barrier coating failure mode under oxidizing environment. *J Eng Gas Turb Power* 2009, **131**: 022101.
[132] Li GR, Yang GJ, Li CX, *et al.* Sintering characteristics of plasma-sprayed TBCs: Experimental analysis and an overall modelling. *Ceram Int* 2018, **44**: 2982–2990.
[133] Rätzer-Scheibe HJ, Schulz U. The effects of heat treatment and gas atmosphere on the thermal conductivity of APS and EB-PVD PYSZ thermal barrier coatings. *Surf Coat Tech* 2007, **201**: 7880–7888.
[134] Hu YP, Ru Y, Zhou XC, *et al.* Correlating microstructure recovery to rejuvenation of high-temperature creep properties in a crept single-crystal superalloy. *Mater Res Lett* 2024, **12**: 217–225.
[135] Petrushin NV, Elyutin ES, Visik EM, *et al.* Development of a single-crystal fifth-generation nickel superalloy. *Russ Metall-Metall* 2017, **2017**: 936–947.
[136] Perrut M, Caron P, Thomas M, *et al.* High temperature materials for aerospace applications: Ni-based superalloys and γ-TiAl alloys. *Cr Phys* 2018, **19**: 657–671.
[137] Yang L, Liu QX, Zhou YC, *et al.* Finite element simulation on thermal fatigue of a turbine blade with thermal barrier coatings. *J Mater Sci Technol* 2014, **30**: 371–380.
[138] Tang WZ, Yang L, Zhu W, *et al.* Numerical simulation of temperature distribution and thermal-stress field in a turbine blade with multilayer-structure TBCs by a fluid–solid coupling method. *J Mater Sci Technol* 2016, **32**: 452–458.
[139] Wei ZY, Cai HN, Tahir A, *et al.* Stress states in plasma-sprayed thermal barrier coatings upon temperature cycling: Combined

effects of creep, plastic deformation, and TGO growth. *Ceram Int* 2019, **45**: 19829–19844.
[140] Wei ZY, Cai HN, Feng RX, *et al*. Dynamic crack growth mechanism and lifetime assessment in plasma sprayed thermal barrier system upon temperature cycling. *Ceram Int* 2019, **45**: 14896–14907.
[141] Li GR, Tang CH, Yang GJ. Dynamic-stiffening-induced aggravated cracking behavior driven by metal-substrate-constraint in a coating/substrate system. *J Mater Sci Technol* 2021, **65**: 154–163.
[142] Ashofteh A, Rajabzadeh M. Advances in thermal barrier coatings modeling, simulation, and analysis: A review. *J Eur Ceram Soc* 2024, **44**: 116693.
[143] Jiang JS, Wang WZ, Zhao XF, *et al*. Numerical analyses of the residual stress and top coat cracking behavior in thermal barrier coatings under cyclic thermal loading. *Eng Fract Mech* 2018, **196**: 191–205.
[144] Sfar K, Aktaa J, Munz D. Numerical investigation of residual stress fields and crack behavior in TBC systems. *Mater Sci Eng A* 2002, **333**: 351–360.
[145] Bäker M, Rösler J, Heinze G. A parametric study of the stress state of thermal barrier coatings Part II: Cooling stresses. *Acta Mater* 2005, **53**: 469–476.
[146] Cheng B, Zhang YM, Yang N, *et al*. Sintering-induced delamination of thermal barrier coatings by gradient thermal cyclic test. *J Am Ceram Soc* 2017, **100**: 1820–1830.
[147] Doleker KM, Ahlatci H, Karaoglanli AC. Investigation of isothermal oxidation behavior of thermal barrier coatings (TBCs) consisting of YSZ and multilayered YSZ/$Gd_2Zr_2O_7$ ceramic layers. *Oxid Met* 2017, **88**: 109–119.
[148] Liu XJ, Wang T, Li CC, *et al*. Microstructural evolution and growth kinetics of thermally grown oxides in plasma sprayed thermal barrier coatings. *Prog Nat Sci Mater* 2016, **26**: 103–111.
[149] Shi JQ, Zhang TB, Sun B, *et al*. Isothermal oxidation and TGO growth behavior of NiCoCrAlY–YSZ thermal barrier coatings on a Ni-based superalloy. *J Alloys Compd* 2020, **844**: 156093.
[150] Liu YZ, Zheng SJ, Zhu YL, *et al*. Microstructural evolution at interfaces of thermal barrier coatings during isothermal oxidation. *J Eur Ceram Soc* 2016, **36**: 1765–1774.
[151] Lima RS, Marple BR. Toward highly sintering-resistant nanostructured ZrO_2–7 wt%Y_2O_3 coatings for TBC applications by employing differential sintering. *J Therm Spray Techn* 2008, **17**: 846–852.
[152] Li GR, Wang LS, Yang GJ. A novel composite-layered coating enabling self-enhancing thermal barrier performance. *Scripta Mater* 2019, **163**: 142–147.
[153] Wang N, Zhou CG, Gong SK, *et al*. Heat treatment of nanostructured thermal barrier coating. *Ceram Int* 2007, **33**: 1075–1081.